Study of dielectric properties of (MgCuNiZnCo)O and its Lithium analogues pellets for its potential application as super-capacitor/battery electrolyte

A thesis submitted towards partial fulfilment of the requirements for the degree of:

Master of Technology in Nano Science and Technology

Submitted by:

Soumyajit Das

Roll no. : M4NST23014B

Registration no. : 160445 of **2021-2022**

Under the guidance of

Dr. Chandan Kumar Ghosh

School of Materials Science and Nanotechnology

Jadavpur University

Kolkata – 700032

Course Affiliated to:

Faculty of Interdisciplinary of Studies,Law and Management

Jadavpur University, Kolkata

2023

CERTIFICATE OF RECOMMENDATION

This is to certify that the thesis entitled **"Study of dielectric properties of (MgNiCuZnCo)O and its lithium analogues pellets for its potential application as supercapacitor/battery electrolyte "** is an authentic work carried out by **Soumyajit Das** under our supervision and guidance for partial fulfilment of the requirement for Post Graduate Degree of Master of Technology in Nano Science and Technology during the academic session 2022-23.

THESIS ADVISOR

Dr. Chandan Kumar Ghosh

School of Materials Science and Nanotechnology

Jadavpur University,

Kolkata-700032

Director

School of Materials Science and Nanotechnology

Jadavpur University,

Kolkata-700032

DEAN

Faculty Council of Interdisciplinary Studies, Law and Management

Jadavpur University,

Kolkata-700032

CERTIFICATE OF APPROVAL **

This foregoing thesis is hereby approved as a credible study of an engineering subject carried out and presented in a manner satisfactorily to warranty its acceptance as a prerequisite to the degree for which it has been submitted. It is understood that by this approval the undersigned do not endorse or approve any statement made or opinion expressed or conclusion drawn therein but approve the thesis only for purpose for which it has been submitted.

Committee of final examination ---

for evaluation of Thesis ---

** Only in case the thesis is approved.

DECLARATION OF ORIGINALITY AND COMPLIANCE OF ACADEMIC ETHICS

I, Mr. Soumyajit Das hereby declare that this thesis contains literature survey and original research work by me, as part of partial fulfilment of the requirements for the degree of Master of Technology in Nano Science and Technology during academic session 2022-2023.

All information in this document has been obtained and presented in accordance with academic rules and ethical conduct.

I also declare that, as required by this rules and conduct, I have fully cited and referred all material and results that are not original to this work.

Signature : Date :

Dedicated to my family

ABSTRACT

Entropic contributions to the stability of solids are very well understood and the mixing entropy has been used for forming various solids, for instance such as rocksalts. A particular development was related to high entropy alloys in which the configurational disorder is responsible for forming simple solid solutions and which are thoroughly studied for various applications especially due to their mechanical properties, electrical properties, hydrogen storage, magnetic properties. Many unexplored compositions and properties still remain for this class of materials due to their large phase space. In this thesis, it was shown that to prepare five equimolar binary oxides yield, after heating at high temperature and quenching, an unexpected rock salt structure compound with distribution of the cations in a face centered cubic lattice. Following this seminal study, here that these high entropy oxides can be substituted by aliovalent(Li - 5%,7.5%,10%) elements with a charge compensation mechanism. This possibility largely increases the potential development of new materials by widening their phase space. Here the aliovalent substitution of 7.5% lithium doped HEOx composition exhibits colossal dielectric constants of 1 x $\mathbf{10^5}$ order at 423k around 70Hz, which could make it very promising for applications as large-*k* dielectric materials.

Keywords- Colossal Dielectric constant, aliovalency, fcc lattice, charge compensation mechanism

ACKNOWLEDGEMENT

This work described in the thesis titled "**Study of dielectric properties of (MgNiCuZnCo)O and its lithium analogues pellets for its potential application as supercapacitor/battery electrolyte**" was started in the School of Materials Science & Nanotechnology department laboratory, Jadavpur University in 2022 and would not have been what it is today without the support and advice of others. It was a golden opportunity to work under the guidance of Dr. Chandan Kumar Ghosh, School of Materials Science & Nanotechnology. I sincerely would like to thank him for his support and experienced guidance throughout the project work and for allowing me to utilize the valuable resources and necessary laboratory and library facilities. I accept this opportunity to thank all the members of our department for helping me to carry out some key characterization studies. I am deeply indebted to all my lab members for their invaluable contribution to complete my project work. I also acknowledge the help rendered by every individual who has been there beside me during execution of my thesis work. I take this occasion also to thank all my classmates whose cooperative attitude helped me very much. I would also like to acknowledge the cooperation of all the staff members of department during my project work.

Finally, I pay my indebt acknowledgement to my family for giving me inspiration and supporting me.

Date : Soumyajit Das

CONTENTS

CHAPTER 1: INTRODUCTION

1.1. Definition of Nano Science & Technology

The prefix 'nano' refers to a Greek prefix that means 'dwarf' or very small and represents one thousand millionths of a metre (10^{-9} m). We must differentiate between nanoscience and nanotechnology. Nanoscience is the study of structures and chemicals on nanometer scales ranging from 1 to 100 nm, and nanotechnology is the technology that uses in practical applications such as devices. In comparison, a single human hair is 60,000 nm thick and the DNA double helix has a radius of 1 nm.

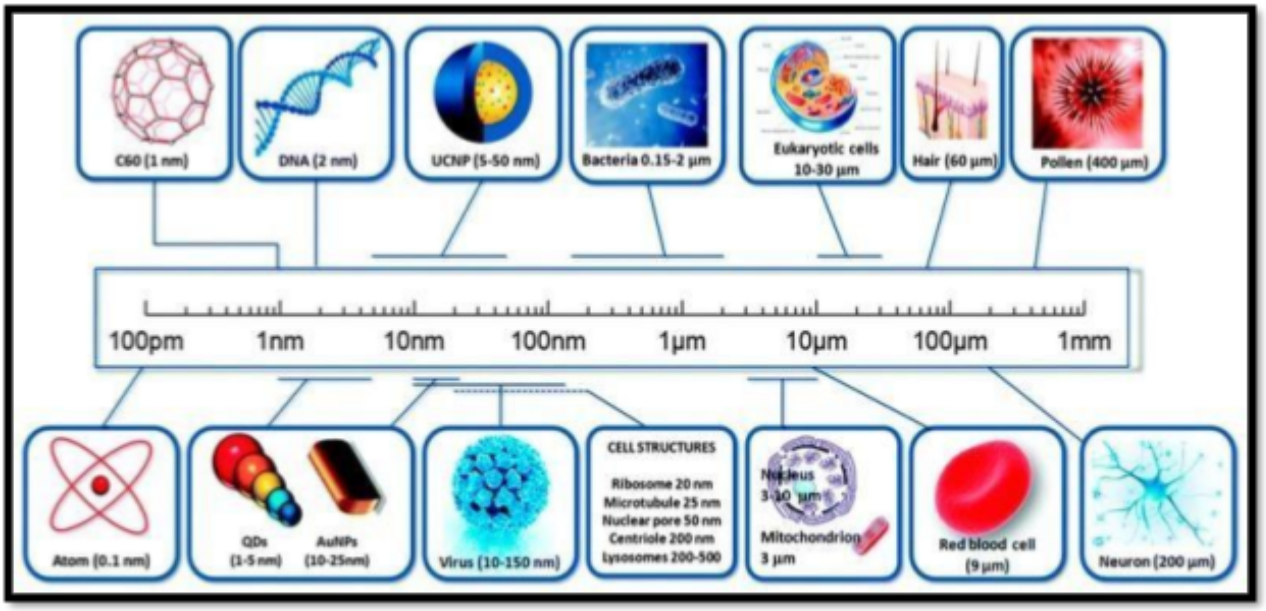

Figure 1: A comparison of sizes of nanomaterial.

Nanotechnology is one of the most promising 21st-century technologies. It is the ability to apply nanoscience theory by viewing, measuring, manipulating, assembling, regulating, and creating materials on a nanoscale scale. Nanotechnology is defined by the National Nanotechnology Initiative (NNI) in the United States as "a science, engineering, and technology conducted at the nanoscale (1 to 100 nm), where unique phenomena enable novel applications in a wide range of fields, from chemistry, physics, and biology, to medicine, engineering, and electronics." Nanoscience is the application of physics, materials science, and biology to the manipulation of materials at the atomic and molecular levels, whereas nanotechnology is the ability to observe, detect, modify, construct, regulate, and manufacture matter at the nanometer scale [3].

Properties of Nanomaterial

1. **Dimension:** at least one dimension ranging from 1 to 100 nanometres (nm).
2. **Methodology:** developed with approaches that demonstrate fundamental control over the physical and chemical properties of molecular-scale formations.
3. **Building block property:** They can be merged to construct larger structures. In general, nanoscience is relatively natural in microbiological sciences because the sizes of many bioparticles dealt with (such as enzymes, viruses, and so on) fall within the nanometer range.
4. **Large area/volume ratio:** The surface area/volume ratio has a greater impact on certain properties of nanoparticles than on bulk particles.
5. **Interfacial layer:** The interfacial layer created by ions and molecules from the medium that are within a few atomic diameters of the surface of each particle for nanoparticles dispersed in a medium of diverse compositions can conceal or change its chemical and physical properties.

That layer is, in fact, an essential component of each nanoparticle.

Applications of Nanotechnology

Nanotechnology is being applied in a wide range of scientific domains, with a wide range of unique applications. When a particle is shrunk to the nanoscale, the properties of the substance change proportionally to its size. As a result, it creates new opportunities in a range of industries. There is greater surface area to react when the surface-to-volume ratio grows with size. The diameter or size of particles influences a variety of optical and mechanical qualities.

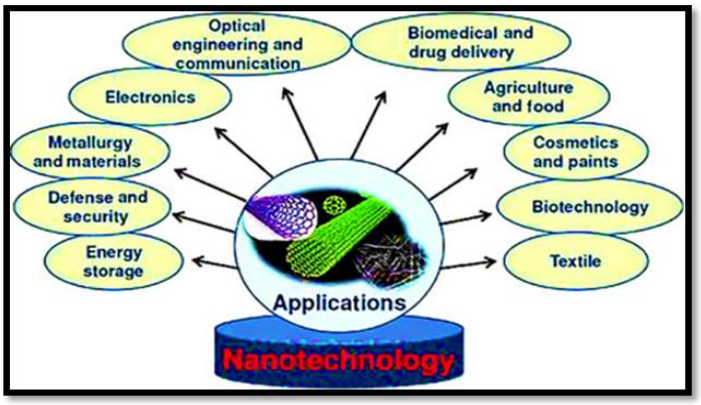

Electronics: In electronics, nanotechnology allows for faster, smaller, and more portabl systems. Nanoelectronics improves electrical device capabilities, boosts memory chip density, and reduces power consumption and transistor size in integrated circuits.

Energy storage: Nanotechnologies, such as novel ceramic, heat-resistant, and still flexible separators and high-performance electrode materials, can significantly improve the capacity and safety of lithium-ion batteries [4].

Biomedical and drug delivery: Nanotechnology applications in several biologyrelated domains, such as diagnosis, medicinal delivery, and molecular imaging, are being extensively explored and yield promising results. In the realm of nano-oncology, remarkable progress has been made in enhancing the efficacy of standard chemotherapeutic medications for a variety of aggressive human tumours [5,6].

Defence and security: Nanomaterials have the potential to make firearms lighter and with more ammunition. When these new technologies are combined, they may lead to guns that can automatically target and fire self-guided rounds if an attacker is identified. Nanorobots are capable of attacking and destroying weaponry, metals, and other objects [7].

Fig. 1.2 - Applications of Nanotechnology

1.2. Introduction to High Entropy Materials

High-entropy alloys (HEAs), also known as multi-principal element alloys, emerged into the academic literature in 2004 and have grown in applications and understanding since. They are multicomponent solid solution materials that contain five or more elements in near-equiatomic proportions to stabilize their structures by maximizing the configurational entropy. These unconventional structures provide opportunities for achieving unprecedented combinations of phase stability and mechanical performance, especially overcoming the strength-ductility trade-off. Although there are still arguments on if these multicomponent alloys are really stabilized by entropy or not, we here call it HEAs for its popularity in the literature . It is believed that the excellent performances of HEAs are promoted by four ‘‘core effects’’: the high-entropy effect, the lattice distortion effect, the sluggish diffusion effect, and the ‘‘cocktail’’ effect, all of which are pivotal to structure-property studies in this field. HEAs are defined from a signature concept, the high-entropy effect, which highlights that when five or more elements are combined they may favor forming of a solid solution over an intermetallic compound .

For our view, the most unique structural character of HEAs is the antisite disordering of atomic types within an ordered crystal. This character could be extended to compounds and other applications. Rost et al. have synthesized rock-salt $(NiCoCuZnMg)O_x$ solid solution oxide and these oxides are named as high-entropy oxides (HEOs) because they are also stabilized by high configurational entropy. Up to now, numerous functional HEOs, high-entropy metallic glass (HEMGs) nanoparticles (NPs) , high-entropy borides (HEBs) , high-entropy sulfides (HESs) , high-entropy carbides (HECs) , and high-entropy nitrides (HENs) have also been developed. High-entropy materials (HEMs) including above compounds, are defined as any solid solution materials that consist of quasi-equimolar multicomponent . Recent works show that HEMs can be utilized for various energy-related applications, as catalysts for ammonia oxidation and decomposition as electrocatalysts for oxidation (methanol)], carbon monoxide, evolution (oxygen], hydrogen), reduction (carbon dioxide , oxygen), and degradation (azo dye]); as electrode for batteries; as hydrogen storage; as supercapacitors; etc. The structural tunability of HEMs provides them a great possibility for energy-related applications. For example, catalytic performances. HEMs for energy-related applications are usually in the form of nanoporous alloys or NPs to maximize their surface areas to prompt the reaction kinetics. Nanosized HEMs can be synthesized with wet-chemistry (solvothermal, ultrasonicated-assisted wet-chemistry, sol-gel auto-combustion, etc.), pulsed laser deposition (PLD), electrodeposition, carbothermal shock (CTS) methods, and so on, where processing

temperature, heating, and cooling rates are key factors to form stable nanosized HEMs. In addition to thermodynamic stability, the uniform configuration of elements with different sizes through a singlephase solid solution also leads to severe lattice distortion, which then increases the activation barrier of diffusion (the sluggish diffusion effect) and improves kinetic stability. The applications of HEMs for catalysis or energy storage have been investigated for less than one decade, and lots of explorations are needed for understanding well their structure-performance correlations.

In this work, we summarize the research progress of energy-related applications of HEMs. After a survey on the syntheses of HEMs, we introduce the structure and theory of HEMs and then the applications of nanosized HEMs, correlating with their structures, as shown in the roadmap of the figure. To keep the article brief, we skip the background knowledge of each application and focus on the structure-performance correlations of HEMs. In the last section, we present our perspectives on the challenges and future research opportunities.

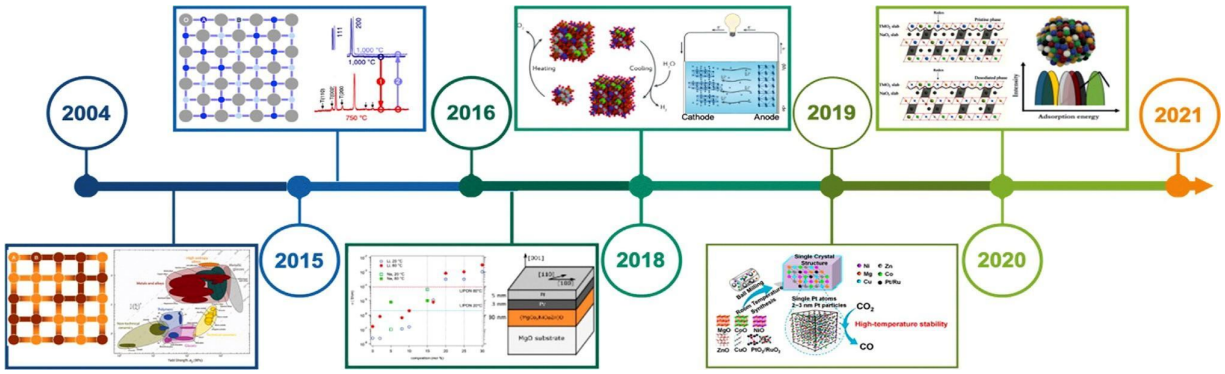

Figure 1. Roadmap of HEMs for recent energy-related applications

Structure High Entropy Oxides

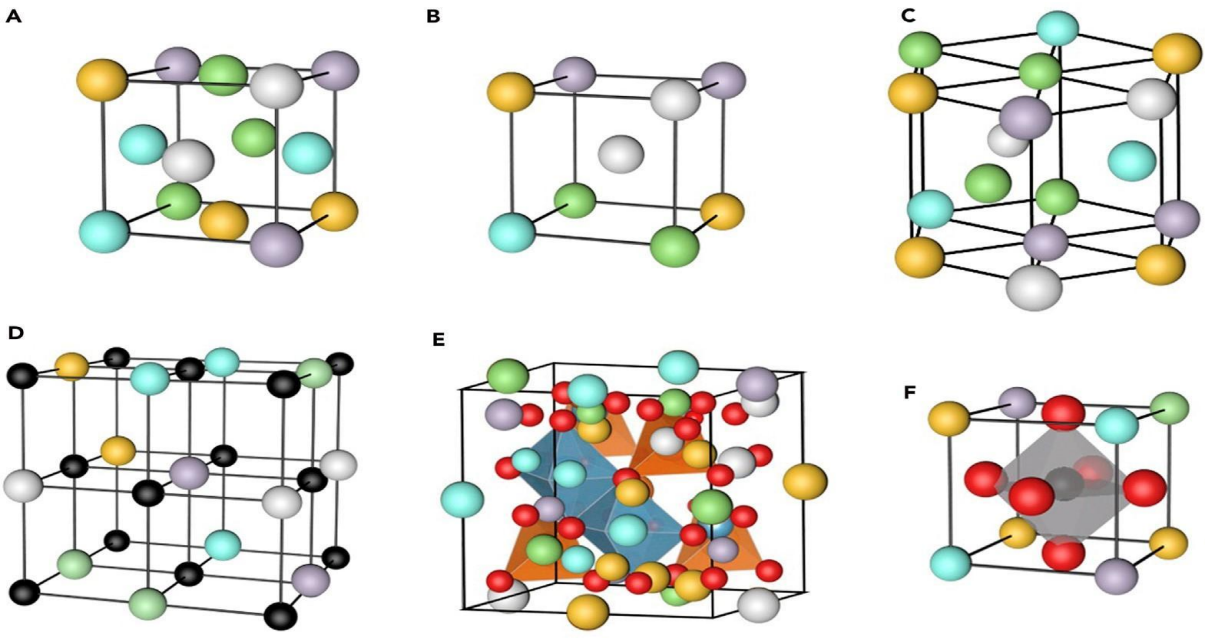

Figure 3. Typical structures of HEAs, HEOs, and other HEMs

(A) fcc lattice structure, (B) bcc lattice structure, (C) hexagonal crystal structure, (D) rock-salt structure, (E) spinel structure, and (F) perovskite structure.

HEOs with fcc lattice constitute a large portion of energy-related applications such as catalysis and battery electrode materials. Among fcc structures, rock-salt HEO of $(MgCoNiCuZn)O_x$ was synthesized. Extended X-ray absorption fine structure and scanning transmission electron microscopy (STEM) analyses reveal that the first-near-neighbor cation-to-anion distances of this compound are identical. With a substitution of Li^+ up to 16.6%, this HEO still keeps its rock-salt structure, shedding potential for energy-storage applications. Recently, this kind of rock-salt HEO exhibits a long-range magnetic order coexisted with the component disorder, and Zhang et al. found that the magnetic order in this HEO might correlate with Cu^{2+} Jahn-Teller distortions through neutron diffraction.

Study has been done on the distortion and atomic disordering of this HEO using X-band electron paramagnetic resonance spectroscopy. They proposed that post-annealing treatment can adjust the local environment of Cu^{2+}, from octahedral in air-quenched Cu-sub-stoichiometric samples to rhombic in Cu-enriched HEOs, and then adjust the Jahn-Teller distortion and the dielectric property . The results agreed with the density functional theory (DFT) calculations by Ra´k et al. Splitting of the Cu d-states near the Fermi level after relaxation suggests a Jahn-Teller distortion involving O-atom, which offers new possibilities of tuning the dielectric, magnetic, superconductivity, etc., properties of HEOs.

HEOs composed of multicomponent rare earth elements as $(Ce,La,Pr,Sm,Y)_2O_{3+x}$ synthesized by NSP method have CaF_2-type structures. Interestingly, Djenadic et al. suggested that they cannot maintain single phase without Ce (such as (Ga, La, Nd, Pr, Sm, Y)O) . In addition, it has been found that $(HfZrCeTiSn)O_2$ with CaF_2 structure exhibits a single phase at high temperature and multiphase at low temperature, which is believed as an evidence of entropy stabilization. It seems that not only the entropy effect but also the compositions affect the structural stabilization of HEOs in addition to the synthesis procedure and the crystal size

🎬 **Applications** :

Mostly HEO is used in energy related applications, especially catalysis and energy storage. HEMs provide a rich platform for tuning the antisite disordering of atoms within a crystalline structure, for achieving an optimized performance. However, the understanding between the performance and surface structure at atomic level is still not clear. The essential task for developing HEMs is to achieve this structure-property relationship and precisely control their structure and local electronic structure. We briefly list several challenges below. With the help

of advanced calculations, synthesis, and characterization tools, these challenges also provide huge opportunities to explore HEMs. Apart from this there are applications that can be given as an breakthrough. As a property superalloys can be used in turbine blades. HEMs have many opportunities in the field of thermal spray technology. The protection layer could improve corrosion, oxidation, thermal, and/or wear resistance of structure parts. One important application is HEA hot working dies which can sustain the extrusion temperature of 1200 °C. For Al alloy extrusion, the maximum extrusion temperature is 500 °C. But, for steels, the typical extrusion temperature is around 1200 °C. High-entropy carbides have the important application for cutting tools. Cutting tools used in machining demand less flank wear and longer lifetime for dry cutting and high-speed cutting.

1.3. Introduction to Supercapacitors

With the rapid growth of the global economy, the depletion of existing fossil fuels and increasing environmental problems, it is utmost important to develop new form of highly efficient, sustainable and eco-friendly energy storage device. Presently electrochemical supercapacitors (ES), rechargeable batteries, fuel cells have attracted considerable interest in both academia and industry as important energy storage devices. Among these supercapacitor is gaining huge attention because of their **fast charging and discharging cycle**, **high power density**, **moderate energy density** and **long cycle life**.

In In today's energy-dependent world, electrochemical devices for energy storage and conversion such as batteries, fuel cells and electrochemical supercapacitors (ESs) have been recognized as the most important inventions among all energy storage and conversion technologies. The electrochemical supercapacitor, also known as a supercapacitor, ultracapacitor or electrochemical double-layer capacitor is a special type of capacitor that can store relatively high energy density compared to storage capabilities of conventional capacitors. ES devices posses several high impact characteristics such as fast charging capabilities, long charge- discharge cycles and broad operating temperature ranges. As a result, their use in hybrid and electrical vehicles, electronics, aircraft and smart grids is widespread. Although ES systems still face some challenges, such as relatively low energy density and high cost, further development will allow ES to work as power devices in tandem with batteries and fuel cells and also function as stand-alone high energy storage devices. For energy storage devices, energy density and power density are very important parameters for characterizing the performance of the devices. Energy density defines the amount of energy that can be stored in a given volume of weight of the material. Power density defines the total energy per unit time which can be stored into the device. So, the ideal storage device should have both high energy density and high-power density. To compare the energy and power capabilities a representation known as the Ragone plot or diagram has been developed has been shown in the figure. Batteries have high energy density, but poor power density. Fuel cells have the highest energy density and lowest power density. By contrast with them, supercapacitors could posses high power density and notable increased high energy density. Supercapacitor is also known as electric double-layer capacitor (EDLC), super condenser, pseudo capacitor or ultracapacitor. Compared to conventional electrolytic capacitors the energy density is typically in the order of hundreds of times greater in supercapacitors. In comparison with conventional batteries or fuel cells, EDLCs also have

much higher power density. The present energy crisis has created a growing demand for efficient, portable and high-power energy storage devices. Super capacitors are fast emerging as a promising potential solution to this problem.

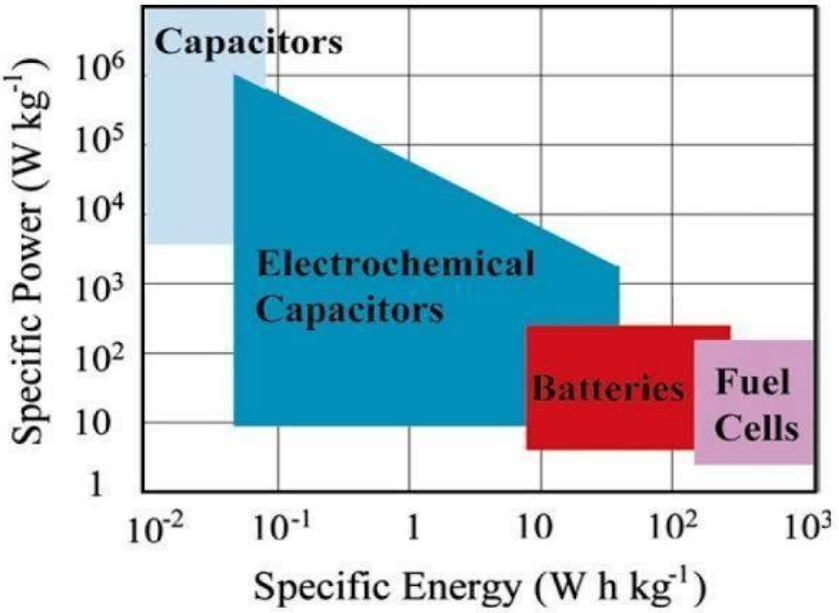

Fig. 1.6 - Ragone plot

Supercapacitors that are fabricated with carbon based electrode offer very low contact resistance and large surface area. These kinds of electrode mainly store charges via the formation of electrostatic double layer which increase the overall performance of the device but cannot store huge amount of charges. However, metal oxides like RuO_2, MnO_2, NiO, CuO etc. which store charges via faradaic mechanism, demonstrate very poor conductivity towards electron conduction. This results in an increase of overall resistance of the electrode reducing the power delivery. In order to address the issues of conductivity, cycling stability researchers have tried to form Lithium doped multiple ion entropy stabilised oxide that give superconductivity..

1.3.1 Fundamentals of Electrochemical Supercapacitor (ES)

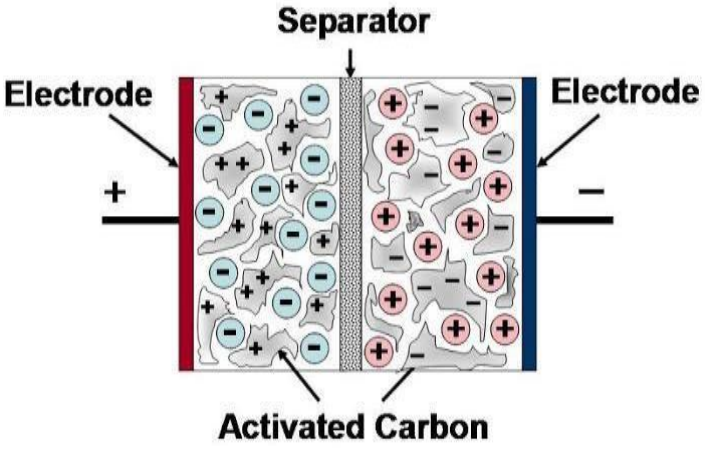

Fig. 1.7 - Design of supercapacitor (EDLC)

An ES consists of two electrodes, an electrolyte, a separator that electrically isolates the two electrode and two highly conductive current collector to enhance electron transport. In general, the ES electrodes are fabricated using nanomaterials which have high surface area and high porosity. Fig.1.7 shows that the charges can be stored and separated at the electrode-electrolyte interfaces which can be treated as a capacitor with an electrical double layer capacitance is expressed as equation (1.1),

$$C = \frac{A\,\varepsilon_0\,\varepsilon_r}{d} \tag{1.1}$$

where A is the area of the electrode surface, ε_r and ε_0 is the dielectric constant of electrolyte and free space respectively and d is the effective thickness of the electrical double layer.

Parameters of ES :

a) **ES Capacitance** :

ES can be treated as two capacitors in series. Since both electrode-electrolyte interfaces represent a capacitor. Total capacitance (C_T) of the entire cell can be expressed as equation (1.2),

$$\frac{1}{C_T} = \frac{1}{C_1} + \frac{1}{C_2} \tag{1.2}$$

where C_1, C_2 are the capacitance of the positive and negative electrode.

b) **Energy Density** :

The energy density of ES is the energy stored per unit volume which can be expressed as equation (1.3),

$$E = \frac{1}{2} C V^2$$

(1.3)

c) **Power Density** :

Power density is the measure of power output per unit volume. It can be expressed as equation,

$$P = \frac{V^2}{4 W_T R_S} \quad (1.4)$$

where R_S stands for equivalent series resistance of ES, W_T is the total weight of the device and V is the cell voltage.

d) **ESR** :

Equivalent series resistance (ESR) is the sum of intrinsic resistance of the electrode material and electrolyte solution, mass transfer resistance of the ions and contact resistance between current collector and the electrode. To achieve a high power density it is necessary to use an electrolyte with high ionic conductivity (i.e. low ESR) and wide operating potential window.

e) **Cycle Life** :

Cycle life is a necessary indicator of the stability of the ES. Stability analysis compares the initial and final capacitance of the electrode undergoing charge and discharge cycling in a certain electrolyte.

f) **Self Discharge Rate** :

Self discharge rate is related to potential losses of a charged electrode over a period of storage time. During the self discharge process, current leakage leads to a decrease of the cell voltage, which in turn may restrict the use of ES.

g) **Thermal Stability** :

Currently ES has working temperature range of -30^{0}C to 70^{0}C, therefore widening the operation temperature range allow us to introduce more application domain

1.3.2 Types of Supercapacitors & its Charge Storage Mechanism

Based upon present scenarios, supercapacitors can be divided into three general classes: electrochemical double-layer capacitors, pseudo capacitors and hybrid capacitors. Each class is characterized by its unique mechanism for storing charge. These are respectively, non-Faradaic, Faradaic and a combination of the two. Faradaic processes,such as oxidation-reduction reactions, involve the transfer of charge between electrode and electrolyte. A non-Faradaic mechanism, by contrast, does not use a chemical mechanism. Rather charges are distributed on surfaces by physical processes that do not involve the

making or breaking of chemical bonds. A graphical taxonomy of the different classes and subclasses of supercapacitors is presented in the below figure.

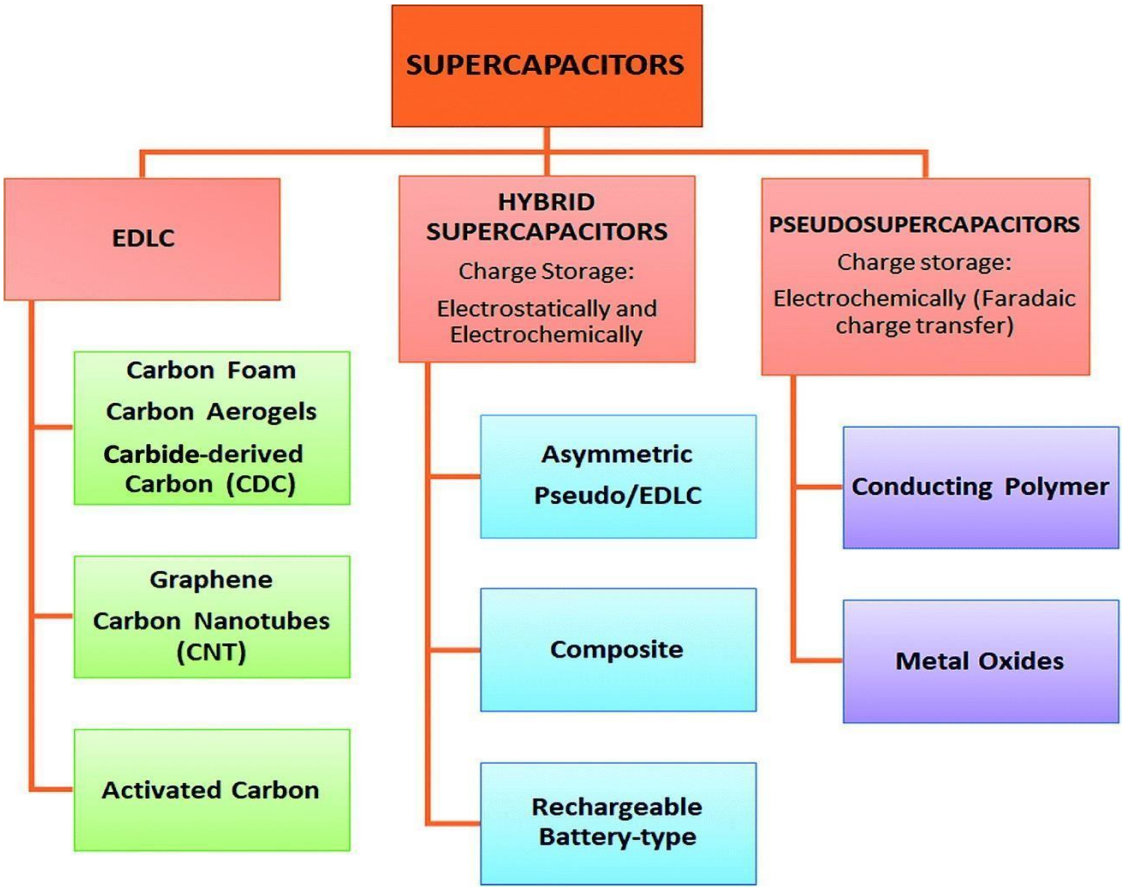

a) EDLC : When an electrically conductive electrode is immersed in an ion conductive electrolyte solution, a double layer spontaneously forms due to the accumulation of charges. An EDLC **(**Fig.1.7) is the simplest supercapacitor, where the charge is physically stored by transfer occurs.

The concept of the existence of the double layer at the surface of a metal being in contact with an electrolyte was proposed by Helmholtz in 1879. It was the first theoretical model which assumed the presence of a compact layer of ions in contact with the charged metal surface. The Gouy and Chapman model suggested the involvement of a diffuse double layer in which the accumulated ions, due to the Boltzmann distribution, extend to some distance from the solid surface. In 1924, Stern suggested that the electrified electrode-electrolyte interface includes both the Helmholtz layer and the diffuse layer. In 1947, Graham pointed out the specific adsorption of ions according to their distance of closest approach at the metal surface. In consecutive developments, it became clear that the dipolar solvent must interact with the charged metal surface. Parsons showed that the dielectric constant of the solvent in

the compact layer of adsorbed molecules is much lower compared to the outer region and approaches the limiting Maxwell value.

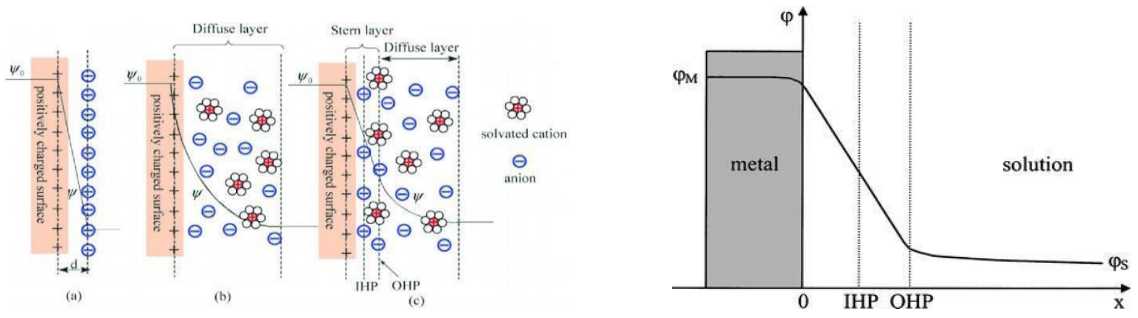

Fig. 1.8 - Change in the electric potential within the double layer

The change in the electric potential within the double layer is shown in Fig.1.8. Two planes are basically associated with the double layer. The inner Helmholtz plane (IHP), passes through the centers of specifically adsorbed ions and the outer Helmholtz plane (OHP), passes through the centers of hydrated ions which are in contact with the metal surface. The electric potentials linked to IHP and OHP can be written as ψ_2 and ψ_1 respectively. The diffuse layer is developed outside the OHP. The concentrations of cations in the diffuse layer decreases exponentially with the distance from the electrode surface. It is considered that the electrode is charged negatively. The electric potential ϕ_M is practically constant throughout the metallic phase except for the layers located near to the electrolyte solution, where a discontinuity in the metal structure occurs and the wave properties of the electron are found (the jellium model).

The thickness of the electric double layer is usually represented in terms of Debye Huckel length (k^{-1}) :

$$k^{-1} = \left(\frac{\varepsilon_r \, \varepsilon_0 \, k_B \, T}{2c^0 \, z_i^2 \, e^2} \right)^{1/2} \qquad (1.5)$$

Where c^0 is the bulk concentration of the z:z electrolyte, ε_r and ε_0 is the dielectric constant of electrolyte and free space respectively, T is the temperature, z_i is the ion charge, e is the elementary charge. Higher concentration and ion charge results reduced thickness of the double layer. The thickness of the double layer is also depend on the potential difference between electrode potential and the potential of zero charge that means larger the potential difference, smaller is the Debye Huckel length.

- **Limitations :** Experimentally the specific capacitance of pure carbon based EDLC is small due to the finite conductivity, unavailability of all of the surface sites and the limited ion

accessibility of the porous structure. As a result, supercapacitors based on EDLC electrode materials can store energy in the range of 3-10 Wh kg^{-1}.

b) Pseudocapacitor : To increase the capacitance of ESs , some electrochemically active materials are investigated for electrode use to provide much higher pseudocapacitance than double layer capacitance. For pseudocapacitance, a faradaic charge transfer in the electrode porous layer occurs through a thermodynamically and kinetically favoured electrochemical oxidation-reduction (redox) reaction. The strong dependency of the change in charge quantity (dq) on electrode potential (dv), represented as $\left(\frac{dq}{dv}\right)$ is called the pseudocapacitance created by the redox reaction. The electrochemical reversibility of employed redox material in a pseudocapacitor normally depends on the structural and chemical reversibility of the reaction mechanism.

Three types of faradaic processes occur in the case of pseudocapacitor i) Under potential deposition (UPD) ii) Redox pseudocapacitance iii) Intercalation pseudocapacitance, shown in Fig. 1.9.

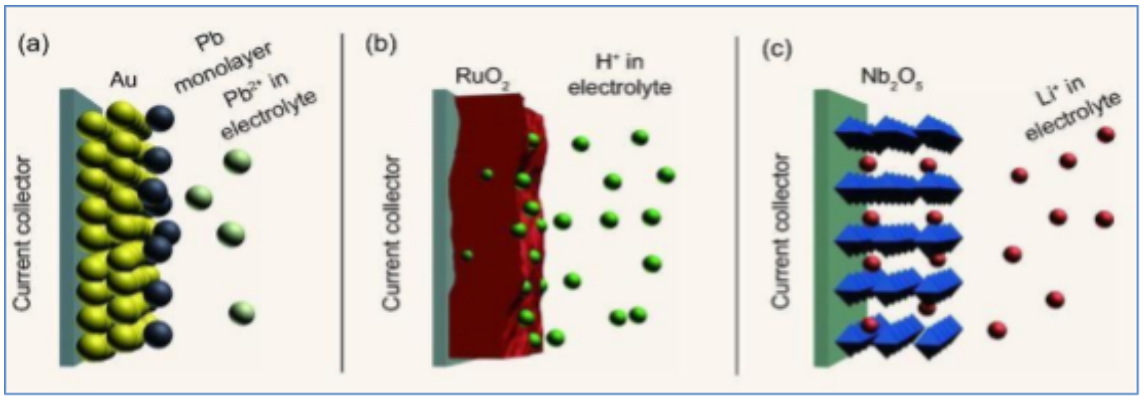

Fig. 1.9 – Pseudocapacitance charge storage mechanisms a) UPD b) Redox pseudocapacitance c) Intercalation

i) Under potential deposition : Under potential deposition is well known for the adsorption of hydrogen atoms on catalytic noble metals such as Au, Pt, Rh, Ru, and Ir. The electrodeposition of metal cations at potentials less negative than their equilibrium potential for cation reduction can be described by equation (1.6),

$$Pb^{2+} + 2e^{-} + 2Au \leftrightarrow 2Au - Pb_{ads} \quad (1.6)$$

The above equation shows the redox reaction of Pb^{2+} on Au electrode surface which is entirely covered by a monolayer of Pb atoms.

The good reversibility of the charge-discharge kinetics is a prime factor in obtaining favourable specific capacitances and power densities for pseudocapacitive materials. However, the operational potential ranges are usually small, only 0.3-0.6 V and the capacitance values are potential dependent for the under potential deposition process. That results limited energy density compared to other pseudocapacitive systems.

ii) Redox pseudocapacitance : Important requirements that should be followed by the redox couples are a) It should exhibit multiple redox states and remain stable over a large potential window. b) It should be very electrically conductive and have accessible structure needed to support performance. c) a high diffusion rate of charge balancing ions within the matrix. Pseudocapacitance based on redox reactions, uses electron transfer between an oxidized species Ox (e.g., RuO_2, MnO_2 or p-doped conducting polymers) and a reduced species, Red (e.g., $RuO_{2-z}(OH)_z$, $MnO_{2-z}(OH)_z$, or n-doped conducting polymers). These reactions are usually described as electrochemical adsorption of cations on the oxidized species surface accompanying fast and reversible electron transfer across the interface between the electrode and the electrolyte, as illustrated in equation (1.7),

$$Ox + zC^+ + ze^- \leftrightarrow RedC_z \tag{1.7}$$

where C^+ (H^+ , K^+ , Na^+ etc.) is the surface adsorbed electrolyte cation and z is the number of transferred electrons.

iii) Intercalation pseudocapacitance : Pseudocapacitance can also occur in the case of ion insertion or intercalation into layered crystalline materials as illustrated in equation (1.8),

$$MA_y + x\,Li^+ + xe^- \leftrightarrow Li_xMA_y \tag{1.8}$$

where MA_y is the layer-lattice intercalation host material (e.g., Nb_2O_5 , MoS_2, TiS_2) and x is the transferred electrons number. The intercalation is accompanied by a change of metal valence to maintain electrical neutrality. The cathode intercalation mechanism requires a faradaic charge or driving force for the lithium cation to adsorb and deposit into the cathode material lattice structure. The electrochemical performance of a cation intercalation pseudocapacitor is described as “transitional” behaviour between Li-ion batteries and supercapacitors. The intercalation pseudocapacitance is characterized by fast ion transport kinetics, short charge time, high rate capability, and long cycling stability, whereas battery materials are limited by solid-state diffusion, resulting in lower power density.

c) Hybrid Capacitor : Hybrid capacitors attempt to exploit the relative advantages and mitigate the relative disadvantages of EDLCs and pseudocapacitors to realize better

performance of the devices. Utilizing both Faradaic and non-Faradaic processes to store charge, hybrid capacitors have achieved energy and power densities greater than EDLCs without sacrificing the cycling stability and affordability that have limited the success of pseudocapacitors. Research has been focused on three different types of hybrid capacitors, distinguished by their electrode configuration: composite, asymmetric and battery-type respectively.

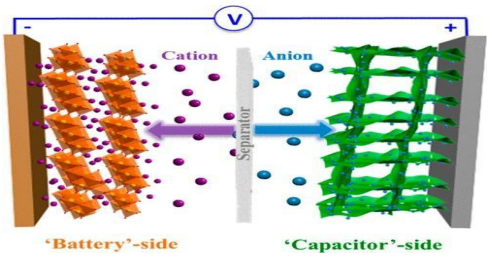

Fig. 1.10 - Design of hybrid capacitor

In designing hybrid ES devices, asymmetric configuration (e.g. one electrode consists of electrostatic carbon material while the other consists of faradaic capacitance material) seems feasible is shown in Fig.1.10. To obtain superior electrochemical performance characteristics, it is important to select separate anode and cathode materials that exhibit extended voltage stability, higher capacitance and higher energy, and power densities.

Application of Supercapacitors

- **Automobile:** One of the most important and widely industry-based application of supercapacitor is automobile vehicles. Due to the crisis of fossil fuel, the world is now directing towards electrical vehicles (EVs). Hybrid electric vehicles (HEV) and pure electrical vehicles (PEV) have become popular and near main stream automobile industry in recent years. Both of these vehicles contain an electrical machine for propulsion purpose. When the vehicle starts to move off, some initial power is required by the motor can be several times of average power demand. Because of this impulsive power, both input and output power capability should be higher. High powered Li-ion batteries are having great energy density but has limited output power capability. Supercapacitors come into the scene as a solution due to its good input and output power density or capability. Therefore, supercapacitors play a huge and important role in automobile industry.

- **Mobile Device** - Supercapacitors can take on different physical forms so that it can be

used in a smaller and thinner version of it. Some new generation mobile phones or devices use xenon flash which is inbuilt into the phone camera to enable good quality photo when light is dim. This flash requires huge power in an instant. If the mobile should be capable of dealing with this power consumption it would have to be unnecessarily bulk and heavy, failing to which leads to short battery life. To resolve this issue some of the brand in mobile industry use supercapacitors to supply the surged power using voltage from the existing battery which decrease the load of main battery and maintain the over all load same as previous. For example, during the flash on situation, overall battery current can be suppressed at 0.2A while the flash may have current up to 4A. As a result, the battery does not have to be large to cater to temporal high-power demands.

- **Micro-Grid** - The micro-grid is called as a possible next generation energy network. It consists of electrical power generation units as well as electrical energy storage components. Popular electrical power generator includes photovoltaic cell, wind turbine, fuel cell and micro turbine while commonly used electrical energy storage units would be the supercapacitor and batteries. As the micro-grids can be inter-connected to the power grid, it is able to supply or demand power from the power grid. At times this configuration is known as the smart grid. The micro-grid has the capability of reducing carbon emission through green energy harnessing as well as having the capability of providing self-sustainable energy. Thus, it is regarded as a contender for the next generation energy network.

🎬 Discussions on different charge storage mechanism by the concept of Cyclic Voltammetry (CV) and Galvanostatic Charge Discharge (GCD) analysis :

Faradaic and non-Faradaic both of these processes are characterized by a current (i) that is directly proportional to the charge-discharge rate (v).

$$i = a\, v^b \tag{1.9}$$

Here a, b are adjustable parameters. Whereas the value of b equals to 1 and 0.5 specifies capacitive and diffusion controlled process respectively.

In the case of EDLC rectangular cyclic voltammogram with a voltage independent current and a linear triangular shaped charge-discharge curve as shown in Fig.1.11 a),b),c).

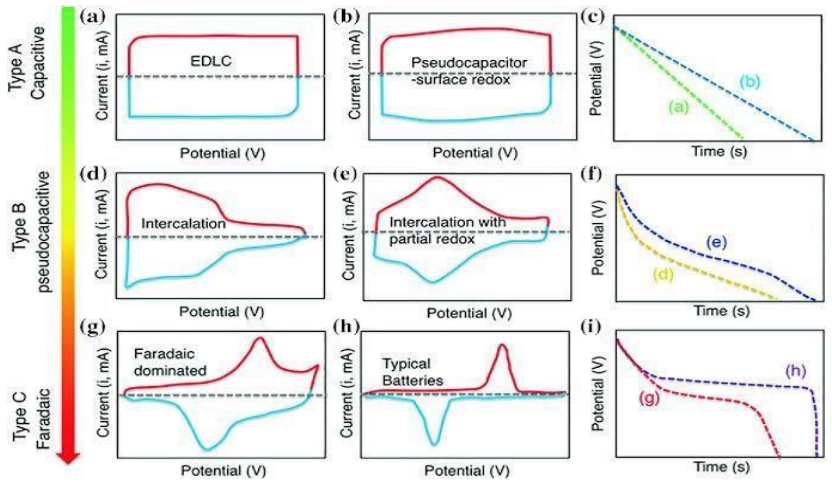

Fig. 1.11 – Schematic cyclic voltammogram & corresponding discharge curves for different energy storage materials

Fig.1.11 d),e),f) shows behaviour involving voltage dependent electrochemical charge transfer i.e. faradaic reaction in pseudocapacitive material which signifies a charge storage mechanism centered between EDLC and battery like ESs.

Fig.1.11 g),h) shows prominent and widely separated peaks associated with the oxidation and reduction of the metal storage (i.e. battery type).

Fig.1.11 i) shows variation of potential with respect to time for the discharge of a battery. The relation is found very nonlinear and characterized by plateaus of nearly constant potential.

1.3.3 Choice of Electrode and Electrolyte

Electrode :

ES device performance is strongly depends on the choice of the electrode materials and electrolytes. Several materials, such as carbon materials (e.g., Activated carbon, Carbon nanotubes, carbon aerogels and graphene etc.), faradaic materials (transition metal oxide, metal hydroxides, metal sulphides and conducting polymers), have been widely investigated as promising electrode materials for ESs. Additionally, metal coordination electrode materials, such as MOFs, PB/PBAs and POMs have been introduced recently.

Carbon materials :

Carbon materials are the most used electrode materials in fabrication of supercapacitor owing to their high surface area, high mechanical strength, high thermal and electrochemical stability, low cost, availability, established electrode production technologies. Usually, carbon materials store charges electrostatically in the double layer. Therefore the capacitance primarily depends on the surface area accessible to the electrolyte ions. To improve the specific capacitance of carbon materials it is essential to consider the effect of high specific surface area and appropriate pore size distribution, pore shape and structure, surface functionality and electrical conductivity. The presence of functional groups on the surface of carbonaceous materials may introduce faradaic redox reactions, leading to a 5-10% increase in the total capacitance. Usually the measured value of specific capacitance of carbon materials in real ESs are in the range of 75-175 F g^{-1} for aqueous electrolytes and 40-100 F g^{-1} for organic electrolytes.

Faradaic materials :

Pseudocapacitive materials store charge through fast, reversible surface redox reactions and hence exhibit considerably large capacitance values (300-2000 F g^{-1}). This category usually includes transition metal oxides, metal hydroxides, metal sulphides and metal nitrides, such as RuO_2, IrO_2, MnO_2, NiO, Co_2O_3, SnO_2, V_2O_5, MoO and $NiCo_2O_4$, MoS_2, $Ni(OH)_2$, $Co(OH)_2$ and conducting polymers (CPs) such as Polyaniline (PANI), Polypyrrole (PPy), Polythiophene (PTh).

In general, metal oxides can provide higher energy density than conventional carbon materials and better electrochemical stability than polymer materials. They not only store

charge electrostatically like carbon materials but also exhibit electrochemical faradaic reactions between electrode materials and ions within appropriate potential windows. RuO_2 is the most studied material because of its wide potential window of 1.2 V, highly reversible redox reactions having three distinct oxidation states, high proton conductivity, remarkably high specific capacitance(720 F g^{-1}) and a long cycle life but their costliness prevents their practical application in ES. But majority of these metal oxides demonstrate very poor conductivity towards electron conduction, which results in an increase of overall resistance of the electrode hampering the power delivery.

The redox reaction in the conducting polymer occurs throughout its entire bulk. During oxidation the ions are transferred to the polymer chain and during reduction the ions are released from this polymer chain into the electrolyte. The processes are highly reversible because the charging and discharging reactions do not involve any structural alterations such as phase changes. Unfortunately, swelling and shrinking of CPs may occur during the intercalating or de-intercalating process which lead to mechanical degradation of the electrode and fading electrochemical performance during cycling, and then limits their usage as electrode materials. To reinforce the stability as well as maximize the capacitance value nanocomposite based electrode materials such as carbon-carbon composites, carbonmetal oxide composites, carbon-conducting polymer composites can also be used.

Metal coordination materials :

Metal coordination materials, including metal-organic frameworks (MOFs), Prussian blue (PB) and its analogues (PBAs), Polyoxometalates (POMs) materials, etc., have been widely used in the field of ESs. They are formed by coordinate bonding between ligands and metal ions.

- Metal organic framework (MOF) :

MOF materials are crystalline comprising metal containing units and organic ligands. Inorganic salts (sulphates, chlorides, and nitrates) and organic ligands (carboxylates, nitriles or azoles) are typically utilized for the metal ion precursor and the organic ligands, respectively. MOFs have higher specific surface areas, larger porosity, variety of structures and functions, as compared with traditional inorganic porous materials. Basically, all sorts of functional materials have been integrated with MOFs to further improve its property. A large number of MOF composites have been successfully synthesized via assembling MOFs combined with carbon materials, conducting polymers, metal doping, hydroxide metal salts, nickel oxalate etc. Thus, MOF (e.g, Co-MOF, Ni-MOF, ZIF 67 etc.) holds great promise as

electrode materials in ESs owing to their controlled pore sizes (0.6-2 nm) as well as their ability to incorporate redox-metal centres.

- Prussian blue (PB) and its analogues (PBAs) :

PB and PBAs have been studied as possible electrode candidates for highly efficient ESs due to their structural superiority, high specific surface area, high porosity, low framework density and high thermal stability as they can realize fast charge and discharge as well as high cycling stability. The chemical formula of PBA materials can be described as $A_xP[R(CN)_6]_{1-y}$ Υ_y,nH_2O (where A is alkali metal or alkaline earth metal, P and R represent the transition metals, Υ is the $[R(CN)_6]$ vacancies, and $0 \leq x \leq 2$, $y < 1$) in which the N-coordinated P cations and C-coordinated R cations in an open framework bridged by cyanide groups.

Thus, the structures and electrochemical properties of PBA materials can be modulated via selecting various combinations of P and R transition metals. There exist two type of transition metal ions in the lattice framework. When P is a transition metal such as Ni, Cu, Zn, N-coordinated P is electrochemically inert, and only C-coordinated Fe^{2+} can undergo redox conversion. Owing to the single active redox site (one electron transfer Fe^{2+}/Fe^{3+}), this type of PBAs shows a low theoretical specific capacity, excellent electrical conductivity, good cycling stability and rate performance. When P is Fe, Co, Mn, etc., there exists two types of redox reaction sites (two electron transfer), i.e., Fe^{2+}/Fe^{3+} and P^{2+}/P^{3+}, leading to higher capacity delivery but with poor cycle stability. To achieve both higher cycling stability and capacity delivery PBA based composite materials (i.e., CoNiHCF, MnFeHCF etc.) are used.

- Polyoxometalates (POMs) :

A new class of faradaic electrode materials known as POMs is emerging as a prime candidate in the field of energy storage systems. POMs are nanometric oxide clusters with reversible redox activities that can be used as building blocks for energy storage applications. These materials comprise a 3D framework of redox active molecular clusters that combine oxygen and transition metals (Mo, V, Nb, Ta and W) at their highest oxidation states. Mainly POMs are well suited to achieve a high capacity for energy storage applications because of their fast and reversible multi electron redox reactions.

Electrolyte :

The electrolyte is a significant constituent in supercapacitors. Electrolyte is the conducting solution of electrolyte salt and solvent which plays an important role in transferring and balancing charges between two electrodes in the cell. The electrolytes are classified into various categories (Fig.1.12).

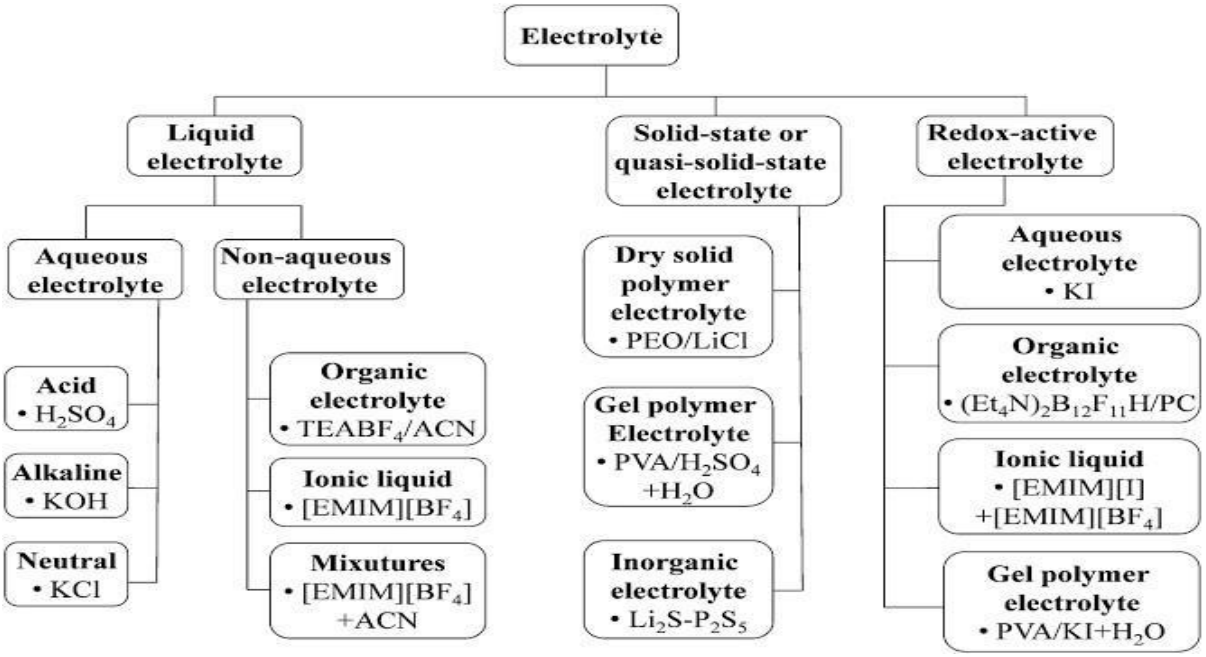

Fig. 1.12 – Types of electrolytes

The interaction between the electrolyte and electrodes in all electrochemical processes significantly influences the electrode-electrolyte interface and internal structure of active materials. The factors influencing the overall performance of supercapacitors are ionic conductivity and mobility, diffusion coefficient, radius of hydrated spheres, solvation, dielectric constant, electrochemical stability, thermal stability and dispersion interaction etc. So the requirements for ideal electrolyte are as follows – a wide electrochemical stable potential window (ESPW), high ionic conductivity, high chemical and electrochemical stability, high chemical and electrochemical inertness to ES components, a wide operating temperature range, well matched with the electrolyte materials, a low volatility and flammability, environmental friendliness, low cost etc.

Aqueous electrolytes :

Aqueous electrolytes have been used extensively in research and development due to their low cost and user friendliness in ES fabrication. Normally, aqueous electrolytes exhibit high

conductivity higher than that of organic and IL electrolytes. It is advantageous for lowering the ESR, leading to a better power delivery of ESs. Aqueous electrolytes are classified into three categories: (a) alkaline, (b) neutral, and (c) acidic solutions. Often used aqueous electrolytes are KOH, NaOH, LiOH, Na_2SO_4, H_2SO_4, $(NH_4)_2SO_4$, K_2SO_4, Li_2SO_4, $MgSO_4$, $CaSO_4$, $BaSO_4$, KCl, NaCl, LiCl, HCl, CsCl, $CaCl_2$, KNO_3, $LiNO_3$, Na_2HPO_4, $NaHCO_3$, $Na_2B_4O_7$ etc. The main disadvantage of aqueous electrolytes is their relatively narrow ESPW (1.0 V to 1.3 V).

Organic electrolytes :

Organic electrolyte based ESs are currently dominating owing to their high operation potential window (2.5 V to 2.8 V) which can provide a significant improvement in both the energy and power densities. Typical organic electrolytes consist of the conductive salts (e.g., tetraethylammonium tetrafluoroborate ($TEABF_4$)) dissolved in the acetonitrile (ACN), acetone, g-butyrolactone (GBL), and propylene carbonate (PC) solvent.

ESs with organic electrolytes usually offer smaller specific capacitance, lower conductivity, and safety concerns related to the flammability, volatility and toxicity. Basically it requires complicated purification and assembling processes in a strictly controlled environment to remove any residual impurities (e.g., water) that can lead to large performance degradation and serious self-discharge issues. The disadvantage of organic electrolytes is their higher resistivity due to their large size molecules which require a large pore size in the electrodes.

Ionic liquids :

The salts composed of ions (organic cations and organic/inorganic anions) with melting points below 100ºC are called ionic liquids (ILs). Due to their unique structures, physical and chemical properties, ILs have received significant importance as alternative electrolytes. The supercapacitor performance can be improved by the tuneability properties of ILs due to their large variety (virtually unlimited) of combinations of cations and anions. Ionic liquids have various advantages such as non-flammability, higher thermal and electrochemical stability, high voltage window (3.5 V to 4 V) and insignificant volatility as compared to organic electrolytes.

ILs can be classified into protic, aprotic and zwitter ionic types based on their composition. ILs used for ESs are based on ammonium, sulfonium, imidazolium, pyrrolidinium and phosphonium cations and hexafluorophosphate (PF_6), tetrafluoroborate (BF_4), bis(trifluoromethanesulfonyl)imide (TFSI), bis(fluorosulfonyl)imide (FSI), and dicyanamide

(DCA) anions. The solvent free ILs may have an advantage in solving the safety problems associated with those organic solvents, making IL-based ESs favourable for hightemperature applications. Unfortunately, there are several main drawbacks with most ILs, such as high viscosity, low ionic conductivity and high cost, which can limit their application in ESs.

Solid and quasi-solid state electrolytes :

There are three types of polymer based solid electrolytes - solid polymer electrolytes (SPEs), gel polymer electrolytes (GPEs), and polyelectrolytes. GPE based ESs currently dominate due to their higher ionic conductivity than dry SPEs. The weak mechanical strength of some GPEs may lead to internal short circuits, causing safety issues. Dry SPEs normally have lower ionic conductivity and higher mechanical strength than GPEs. The limited contact surface area between solid state electrolytes and electrode materials especially for the nanoporous materials is the main issue which increases the ESR value, reduces the rate performance and results low specific capacitance of ESs.

Redox active gel electrolytes :

A superior method to improve the electrochemical performance of an ES device is to add redox active species to the electrolyte. That maximizes the capacitance and the energy density of the device through reversible faradaic reactions and fast electron transfer at the electrode-electrolyte interface. Numerous redox couples, such as iodides (KI), $K_3Fe(CN)_6$ and Na_2MoO_4 ; organic redox mediators, such as hydroquinone, P-phenylenediamine (PPD) and p-benzenediol ; and methylene blue (MB) ; anthraquinone2,7-disulfonate (AQDS) ; and indigo carmine (IC) have been investigated in solid state gel electrolytes. This approach of adding redox species in gel electrolytes effectively improves the performance of the ES device.

1.4. Introduction to Cyclic Voltammetry

Cyclic voltammetry (CV), a widely used potential-dynamic electrochemical technique, can be employed to perform qualitative and quantitative analysis about surface and solution electrochemical reactions including electrochemical kinetics, reaction mechanism, reaction reversibility and effects of electrode structures on these parameters.

The CV measurement is normally conducted in a three electrode configuration or electrochemical cell containing a working electrode (W), counter electrode (C) and reference electrode (R) as shown in Fig.1.13. In the case of symmetric cell CV measurements can also be performed using a two electrode test cell by connecting both the reference and counter electrode probes of the potentiostat to one electrode of the test cell, while connecting the working electrode to the other electrode of the test cell. The electrolyte in the three electrode cell is generally an aqueous or non-aqueous liquid solution. The basic principles of three electrode electrochemical cell for cyclic voltammetric experiments are :

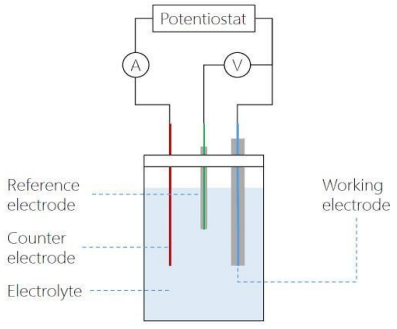

Fig. 1.13 – Electrode configuration for CV experiments

- Reference electrode (R) :

The excitation signal is simultaneously applied across the working and reference electrode. The reference electrode circuit has large resistance so that no current is present in the electrode, therefore providing a stable and reproducible voltage to which the working electrode potential may be referenced. The current that is measured in response to applied potential. Commonly used reference electrodes are aqueous Ag/AgCl, standard hydrogen electrode (SHE) and calomel half cells.

- Counter electrode (C) :

The auxiliary electrode provides the current required to sustain the electrochemical reaction at the working electrode. It is also used to prevent large current from passing through the reference electrode. It is basically non-reactive high surface area electrode, commonly platinum gauze.

- Working electrode (W) :

The working electrode is the electrode through which the potential is "cycled." It is where the electrochemical reaction takes place and therefore, where the current response is also recorded. The working electrode dimensions are kept small to enhance concentration polarization.

- Supporting electrolyte :

A purified supporting electrolyte must be highly soluble in the solvent chosen. It also has to be chemically and electrochemically inert in the conditions of the experiment.

Analysis of CV Curve :

The CV measurement records the current flowing through the working electrode as a function of the applied potential and a plot of current versus potential is observed, which is known as a 'voltammogram'.

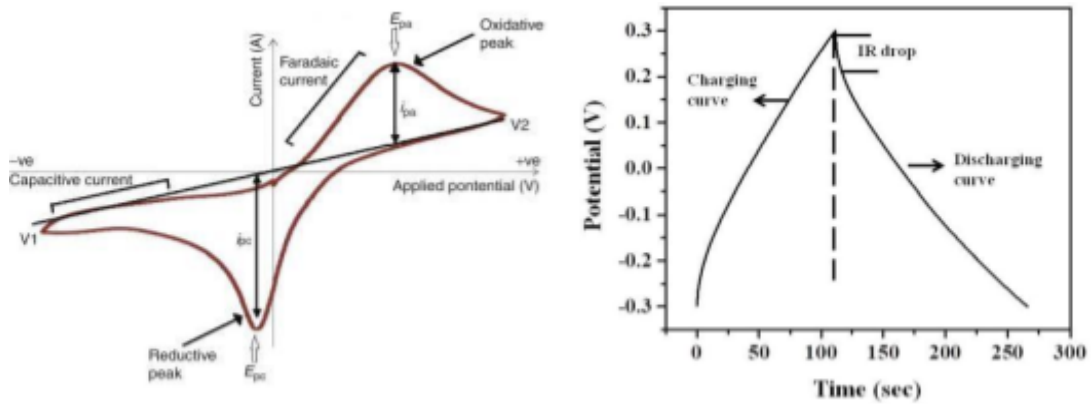

Fig. 1.14 – Typical a) cyclic voltammogram curve and b) galvanostatic charge discharge curve

In the forward scan of working electrode (Fig.1.14.a) the potential first scans positively, from left to right (to positive potential) and later from right to left (to negative potentials) and the current response is measured. The positive scan caused an oxidation of an analyte where the voltage reaches maximum is known as the anodic peak potential (E_{pa}) and results in anodic current (i_{pa}). The reverse negative potential scan caused a typical reduction reaction at the cathodic peak potential (E_{pc}) and results in cathodic current (i_{pc}).

$$I_P = 0.446\, nA\ C_0 \left(\frac{nFvD}{RT}\right)^{1/2} \quad (1.10)$$

For electrochemically reversible electron transfer process the Randles-Sevcik equation (Eq. 1.10) describes how the peak current I_P(A) increases linearly with the square root of the scan rate v (V s^{-1}), where n is the number of transferred electrons in the redox event, $A$is the electrode surface area, D is the diffusion coefficient of the oxidized analyte and C_0 is the bulk concentration of the analyte.

To evaluate material capacitance, we have to measure this working electrode in the chosen electrolyte using electrochemical CV to record cyclic voltammogram of the particular material from which the capacitance (C_m) can be calculated. Where m is the mass of electroactive material and v is potential scan rate.

$$C_m = \frac{i}{2mv} \quad (1.11)$$

And the current (i) which represents the total charge transferred during forward or backward direction CV scanning is obtained by calculating the enclosed area of the CV curves using equation (1.12),

$$i = \frac{\int_{v_1}^{v_2} i(v)\, dv}{(v_2 - v_1)}$$

(1.12)

where v_1 and v_2 are the lowest and highest ends of the potential range.

As mentioned above, the voltage scan rate can affect measured capacitance. At lower scan rate complete redox transition also occurred at inner active sites producing high specific capacitance whereas, the capacitance value decreases at higher scan rate due to limited diffusion effect of electrolyte ion within the electrode layer.

Analysis of GCD Curve :

Galvanostatic charge discharge (GCD) curve is one of the most reliable technique to determine capacitance energy density, power density, equivalent series resistance and cycle life of a supercapacitor.

It can be seen that the charge discharge profile (Fig. 1.14.b) deviate from typical linear variation of voltage with time. It is mainly due to the IR drop that increases with the increase of current rate.

The specific capacitance can be calculated from the GCD profile using equation (1.13),

$$C_m = \frac{i}{\left(-\frac{dv}{dt}\right)} \qquad (1.13)$$

where (i) is the applied current density (A g^{-1}) and $\overline{\frac{dv}{dt}}$ is the average slope of the discharge curve.

The energy density E (Wh kg^{-1}) and power density P (W kg^{-1}) of the supercapacitor can be calculated from the GCD profiles at different current densities using the following two equations (1.14) and (1.15).

$$E = \frac{1}{2}\left[\frac{C_m\,(\Delta v)^2}{3.6}\right]$$

(1.14)

$$P = \frac{3600\,E}{\Delta T}$$

(1.15)

Here C_m is the specific capacitances of the device as obtained from the GCD at different current densities, Δv is the working potential window and ΔT represents different discharge times at different current densities.

Different charging and discharging rates can provide some information about the mass transfer kinetics of an electrode layer. The decrease in specific capacitance with the increasing in current density is due to limited number of interface charges.

Kinetics of Electrochemical Reaction

In this section a quantitative explanation for the influence of the electrode potential on the electrochemical reaction kinetics has been represented.

The following electrochemical reaction determines the dependence of current on electrode potential -

$$Ox + ne^- \leftrightarrow Red^{n-} \qquad (1.16)$$

Where Ox and Red are the oxidized and reduced forms of redox couple and n is the number of electrons participating in redox reaction.

The Nernst equation relates the potential of an electrochemical cell (E) to the standard potential (E^0) and the relative activities of the oxidized (Ox) and reduced (Red) analyte in the system at equilibrium.

$$E = E^0 + 2.303\frac{RT}{nF}\,log_{10}\,(Ox/Red)$$

(1.17)

In the equation (1.17), F is Faraday's constant, R is the universal gas constant, n is the number of electrons, and T is the temperature.

The rate of reduction and the rate of oxidation which is related to the current density ($j =$ I/A i.e, current per unit surface area of electrode) can be written as v_{red} , v_{ox} respectively.

$$v_{red} = k_{red}\, C_O(0,t) = -j_c/nF$$

(1.18)

$$v_{ox} = k_{ox}\, C_R(0,t) = j_a/nF$$

(1.19)

Where j_c and j_a are the partial cathodic and anodic current densities, respectively and $C_O(0,t)$ and $C_R(0,t)$ are the surface concentrations of the oxidized and reduced species at the electrode respectively, at time t.

For any chemical reaction, the rate constant (k) is related to the Gibbs free energy of activation (ΔG) by

ΔG

$$k = Z\, e^{-\frac{}{RT}}$$

(1.20)

Where Z is given by $k_B T\delta/h$ within the framework of the activated complex. Here δ is basically reaction length and k_B is Boltzmann constant, R is universal gas constant and T is the temperature.

In order to overcome the activation barrier and to enhance the desirable reaction an overpotential has to be applied. The reversible behaviour depends on the relative value of standard rate constant (k_s) and mass transport coefficient (k_m).

It has already seen that the electrode reaction is an interfacial reaction that necessarily involves all the processes occurring at the electrode or its vicinity while current flows through the cell. Electrode processes consist of the electrode reactions such as chemical reaction, structural reorganization, adsorption and also the mass transport processes (Fig.1.15) such as diffusion, migration and convection.

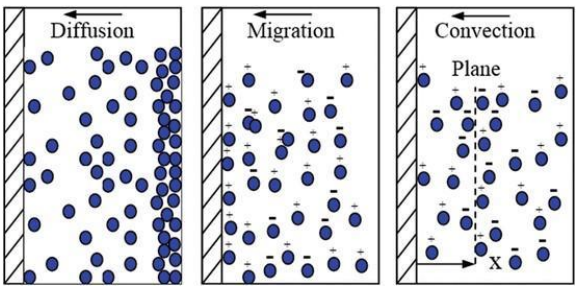

Fig. 1.15 – Different mass transport processes

Mass transport to an electrode can be described by the Nernst-Planck equation (Eq. 1.21). For one-dimensional mass transport along the x -axis, it can be expressed as

$$J_i\,(x) = -D_i\,\frac{\partial c_i}{\partial x} - \left(\frac{z_i F}{RT}\right) D_i c_i\,\frac{\partial \Phi}{\partial x} + c_i\; v(x) \quad (1.21)$$

Where $J_i\,(x)$ is the flux of species i, D_i is the diffusion coefficient, $\Phi(x)$ is the potential at a distance x from the electrode surface, and $v(x)$ is the velocity of a volume element of the solution moving in the x direction. The first term contains the concentration gradient related to the diffusion, the second one expresses the migration related to the motion of charged species forced by the potential gradient and the third term expresses the convection due to the stirring of the solution.

Diffusion should always be considered because concentration gradients between the vicinity of the electrode and the bulk solution originate, which will lead the reactant species to move in the direction of the electrode surface and product molecules (ions) to leave the interfacial region.

1.5. Introduction to Electrochemical Impedance Spectroscopy

As a powerful method, electrochemical impedance spectroscopy (EIS) is used to analyse electrical characteristics of the electrochemical system. Any electrochemical supercapacitor (ES) can be represented in terms of an equivalent electrical circuit that comprises a combination of the double layer capacity (C_d), the impedance of the faradaic or non-faradaic process and the high frequency resistance (R_Ω), constant phase element and Warburg impedance (W) corresponding to the diffusion of the charged particles. A quasi-reversible charge transfer is considered with the equivalent Randles circuit in EIS measurement as shown in Figure 1.16.a.

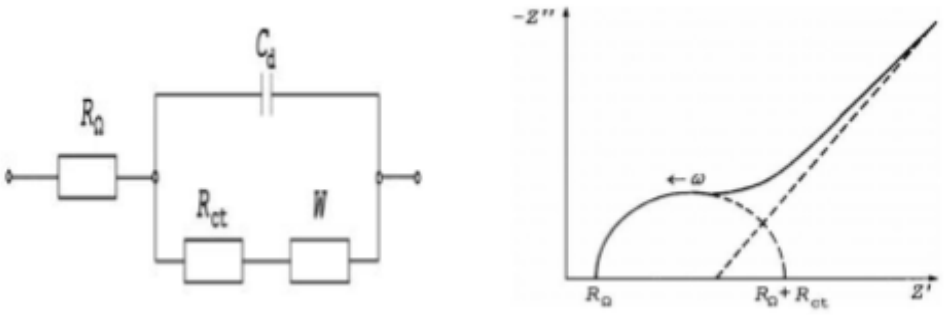

Fig. 1.16 – a) Scheme of the Randles equivalent circuit and b) the corresponding Nyquist Plot

EIS measurement is collecting the ES impedance data at the open circuit potential by applying a small perturbation of amplitude (±5 mv to ±10 mv) over a wide frequency (f) range from 1mHz to 1MHz. Normally, amplitude and phase shift of the response signal is measured. Capacitance can be calculated using a linear portion of a log|z| vs log|f| curve, which is called the Bode Plot. EIS can also be expressed as a Nyquist diagram (Figure 1.16.b), where the imaginary part of the impedance, Z(f′′) is plotted against the real part of impedance, Z(f').

For an ideally polarized electrode, the impedance consists of the double-layer capacity C_d and the solution resistance R_Ω in series. In the impedance plane plot, a straight vertical line results intersecting the Z(f') axis at R_Ω at an angle smaller than 90º to the real axis. When a charge transfer proceeds at the electrode, the equivalent circuit consists of C_d and the charge transfer resistance R_{ct} in parallel. So the corresponding Nyquist impedance plot represents a semicircular arc.

The complete Nyquist plot shows the Randles impedance with the semicircle at higher frequencies and the straight line at an angle of 45º to the real axis at lower frequencies. Therefore, from the diameter of the semicircle on Nyquist plot, charge transfer resistance can be obtained. The charge transfer resistance R_{ct} is defined as equation (1.22)

$$R_{ct} = \frac{RT}{nFj_0} \quad (1.22)$$

where j_0 is the exchange current density, F is Faraday's constant, R is the universal gas constant, n is the number of electrons, and T is the temperature.

1.6. Objectives

The HEOAs has attracted much attention due to its open 3d network framework with large space and 3d diffusion channels which are conductive to the insertion or extraction of cations. $(MgCuNiCoZn)_{1-x}Li_xO$ undoped and doped with Li- 5%,7.5%,10% has robust framework and exhibits electrochemical activity which is mostly applied to energy storage device like supercapacitors and batteries.

The aim of this thesis is to investigate the recent progress in the field of electrolytes supercapacitor and batteries based on HEO (MgNiCuZnCo)O and its lithium analogues.

The objective can be summarised as :

- Synthesis of (MgNiCuZnCo)O (Li0) and its lithium analogues (Li5,Li7,Li10) and characterizations of the synthesized samples in detail.
- In depth study of dielectric properties of prepared samples which can be used to develop supercapacitor and batteries
- Comparison between prepared samples based on their dielectric performance (relative permittivity, impedance etc.) with the variation of temperature ranging from room temperature to 150°C.

REFERENCE

1. Handbook of Nanotechnology : Bharat Bhushan, Springer, 2004
2. Fundamentals Of Nanoelectronics : George W. Hanson , Pearson Education, 2009
3. Nanostructure and nanomaterials synthesis, properties & applications : Guozhong Cao, Imperial College Press, 2004
4. Introduction to Nano : Basic to Nanoscience and Nanotechnology/ Amretashis Sengupta, Chandan Kumar Sarkar, Springer, 2015
5. Mohammadreza Shokouhimehr, Eric S. Soehnlen, Anatoly Khitrin , Soumitra Basu, Songping D. Huang : Inorganic Chemistry Communications 13 (2010) 58–61

6. Lotfi Boudjema, Ekaterina Mamont v J L J u L v u d Ph pp T s : I . Ch . 2017 56 7598−7601
7. Anxing Zhou, Liwei Jiang, Jinming Yue, Yuxin Tong, Qiangqiang Zhang, Zejing Lin, Binghang Liu, Chuan Wu, Liumin Suo, Yong-Sheng Hu, Hong Li, and Liquan Chen : ACS App . M t . I t f s 2019 11 41356−41362
8. Feipeng Zhao, Yeyun Wang, Xiaona Xu, Yiling Liu, Rui Song, Guang Lu, and Yanguang Li : ACS App . M t . I t f s 2014 6 11007−11012
9. Bingxing Xie, Liguang Wang, Jie Shu, Xiaoming Zhou, Zhenjiang Yu, Hua Huo, Yulin Ma, Xinqun Cheng, Geping Yin and Pengjian Zuo : ACS Appl. Mater. Interfaces 2019, 11, 46705−46713
10. Yuru Ge, Xuan Xie, Jessica Roscher, Rudolf Holze & Qunting Qu : Journal of Solid State Electrochemistry (2020) 24: 3215–3230
11. Electrochemical supercapacitors : Scientific Fundamentals and Technological Applications/ B.E.Conway, Kluwer Academic/Plenum Publishers
12. Guoping Wang, Lei Zhang and Jiujun Zhang : Chem. Soc. Rev., 2012, 41, 797–828
13. Electroanalytical Methods : Fritz Scholz, Springer, 2010
14. J D W b Hu Eu su P d D v d M t : Ch . R v. 2018 118 6457−6498
15. E y St N t s − C p t v Ps ud p t v B tt y-like? : ACS N 2018 12 2081−2083
16. Yang Zhao, Zhongxin Song, Xia Li, Qian Sun, Niancai Cheng, Stephen Lawes, Xueliang Sun : Energy Storage Materials 2 (2016) 35-62
17. Shasha Zheng, Huaiguo Xue, Huan Pang : Coordination Chemistry Reviews 373 (2018) 2–21
18. Yuanlong Shao, Maher F. El-Kady, Jingyu Sun, Yaogang Li, Qinghong Zhang, Meifang Zhu, Hongzhi Wang, B u Du d R h d B. K : Ch . R v. 2018 118 9233−9280 19. Cheng Zhong, Yida Deng, Wenbin Hu, Jinli Qiao, Lei Zhangd and Jiujun Zhang : Chem. Soc. Rev., 2015, 44, 7484
20. Bhupender Pal, Shengyuan Yang, Subramaniam Ramesh, Venkataraman Thangadurai and Rajan Jose : Nanoscale Adv., 2019, 1, 3807
21. Deepak P. Dubal, Nilesh R. Chodankar, Do-Heyoung Kim and Pedro Gomez-Romero : Chem. Soc. Rev., 2018, 47, 2065
22. Noemie Elgrishi, Kelley J. Rountree, Brian D. McCarthy, Eric S. Rountree, Thomas T. Eisenhart and Jil L. D ps y : J. Ch . Edu . 2018 95 197−206
23. Electrochemical Supercapacitors for Energy Storage and Delivery : Aiping Yu, Victor Chabot and Jiujun Zhang : CRC Press
24. Reevaluation of Performance of Electric Double-layer Capacitors from Constant-current Charge/ Discharge and Cyclic Voltammetry : Scientific Reports|6:38568| doi: 10.1038/srep38568
25. Electrochemical Impedance Spectroscopy : Mark E. Orazem & Bernard Tribollet, willey

CHAPTER 2: LITERATURE REVIEW

To achieve better electrochemical performance of supercapacitors, development of new electrode materials, especially nanostructured materials, with exceptional charge storage properties and rate capability is essential. MOF compounds such as HEO & HEOAs are a new class of electrode materials prepared by chemical interaction of organic linkers and metal ions or clusters owing to their properties such as tuneable pore sizes, high surface area, remarkable porosity, and ordered crystalline structures. Now after attaining good space in the electrode spectrum the electrolyte segment is been advanced for new prospectus. Due to the promotion of charge transfer inside its open framework structure and redox behaviour of their metal cations, these nanostructures shows superior electrochemical performance in energy storage device, such as aqueous ion batteries and supercapacitors. Here some of the reviews of past work as electrode on this topic have been discussed briefly.

Berardan et al. in 2016 reported by Impedance spectroscopy measurements evidence superionic Li^+ mobility (>10^{-3} S cm^{-1}) at room temperature and fast ionic mobility for Na^+ (5 × 10^{-6} S cm^{-1}) in high entropy oxides, a new family of oxide-based materials with the general formula $(MgCoNiCuZn)_{1-x-y}Ga_yA_xO$ (with A = Li, Na, K). Structural investigations indicate that the conduction path probably involves oxygen vacancies.

Berardan et al. again in 2017 reported the influence of the synthesis conditions, stoichiometry and post-annealing treatments on the crystal structure of (MgCoNiCuZn)O-based high-entropy oxides have been investigated in details. The particular role of copper in the emergence of a distortion and a disordering of the randomly-distributed rocksalt structure has been evidenced by electron paramagnetic resonance and X-ray diffraction studies. An evolution of the local environment of copper from octahedral in Cu-sub-stoichiometric samples to rhombic in Cu-enriched samples leads to a deviation of the crystal structure from the ideal rocksalt one, which depends on the thermal history of the samples. Besides giving new clues to understand the behavior of this new class of materials, this controllable evolution of the crystal structure offers new possibilities of tuning the functional properties of the (MgCoNiCuZn)O-based compounds.

Sarkar et al. in 2018 shown us that high entropy oxides are very promising materials for reversible electrochemical energy storage. The variation of the composition of the oxides allows tailoring the Li-storage properties of the active material. The incorporation of different elements into HEO offers a modular approach for the systematic design of the electrode material. Additionally, it is shown that entropy-stabilized oxides have high capacity retention and exhibit a de-/lithiation behavior, which is drastically different from classical conversion materials. The new effect is attributed to configurational entropy stabilization of the lattice, which conserves the original rock-salt structure while serving as a permanent host matrix for the conversion cycles. Based on these—necessarily limited—first, but promising results, further investigations toward high entropy oxide electrode materials should be pursued to explore their full potential for energy storage applications.

Qiu N. et al in 2018 has considered $Mg_{0.2}Co_{0.2}Ni_{0.2}Cu_{0.2}Zn_{0.2}O$ as an anode material for lithium ion batteries. The HEO anode provides a high initial discharge specific capacity of about 1585 mAh g-1 and exhibits superior cycling stability. A reversible capacity of 920 mAh g -1 was achieved at 100 mA g-1 after 300 cycles. Ex situ scanning electron microscopy (SEM) and selected-area electron diffraction (SAED) revealed that the surface morphology and microstructure of the HEO anodes were still stable even after long term cycling. The well-mixed cations together with an inactive material (MgO, formed after the initial discharge

process) in the HEO anodes result in a remarkable cycling, rate performance and an applicable reversible capacity with an average voltage of ~0.85V. This work may provide a convenient method for obtaining component-controlled oxide nanostructured materials with high electrochemical performance.

Kheradmanfard et al. had concentrated on the synthesis duration and in hhis study, a novel ultrafast facile green microwave-assisted method was developed for the synthesis of high entropy oxide (HEO) (Mg, Cu, Ni, Co, Zn)O nanoparticles for the first time. The results indicated that all the five metallic elements were uniformly distributed in the single-phase rocksalt structure of the HEO nanoparticles. The particle-size distribution was within the range of 20–70 nm, with the average size of 44 nm. When used as anode materials for Li-ion batteries, the HEO nanoparticles exhibited remarkable lithium storage properties with the impressive stability as was demonstrated during 1000 cycles at 1 A/g. The exceptional advantages of the proposed method in this work, including ultrafast speed (few minutes), low temperature, nanoscale and high-purity products, and low cost, make it an excellent synthesis technique for application in newly developed high-entropy ceramics, particularly for Li-ion batteries.

Triolo C. et al synthesized $Mg_{0.2}Co_{0.2}Ni_{0.2}Cu_{0.2}Zn_{0.2}O$, is gaining significant interest as novel anodes for lithium-ion batteries (LIBs) due to their stable crystal structure and robust lithium-storage properties. In his work, $Mg_{0.2}Co_{0.2}Ni_{0.2}Cu_{0.2}Zn_{0.2}O$ oxides with different morphologies are prepared by electrospinning and solvothermal method and are applied as anode active materials for LIBs. It is found that different morphologies possess different characteristics, namely particle size, particle size range, and defect density, which have a significant effect on the electrochemical behavior. The most active (Mg, Co, Ni, Cu, Zn) ESO shows outstanding electrochemical properties in terms of high reversible capacity (480 mAh g^{-1} at 20 mA g^{-1}), superior rate capability (206 mAh g^{-1} at 2 A g^{-1}), and excellent cycling stability (390 mAh g^{-1} at 500 mA g^{-1} after 300 cycles). The strategy demonstrates the importance of engineering microstructures in tailoring the electrochemical performance.

Hong c. et al. continued the work with **Qiu N.** in extension where extreme fine crystalline materials have been extensively investigated as high-rate lithium-storage materials due to their shortened charge-transport length and high surface area. The pseudocapacitive effect plays a considerable role in electrochemical lithium storage when the electrochemically active materials approach nanoscale dimensions, but this has received limited attention. Herein, a series of $(Mg_{0.2}Co_{0.2}Ni_{0.2}Cu_{0.2}Zn_{0.2})O$ electrodes with different particle sizes were prepared and tested. The ultrafine $(Mg_{0.2}Co_{0.2}Ni_{0.2}Cu_{0.2}Zn_{0.2})O$ nanofilm (3–5 nm) anodes show a

remarkable rate capability, delivering high specific charge and discharge capacities of 829, 698, 602, 498 and 408 mA h g^{-1} at 100, 200, 500, 1000 and 2000 mA g^{-1}, respectively, and a dominant pseudocapacitive contribution as high as 90.2% toward lithium storage was revealed by electrochemical analysis at a high scanning rate of 1.0 mV s^{-1}. This work offers an approach to tune the lithium-storage properties of $(Mg_{0.2}Co_{0.2}Ni_{0.2}Cu_{0.2}Zn_{0.2})O$ by size control and gives insights into the enhancement of pseudo capacitance-assisted lithium-storage capacity.

Mostly works has been done taking this high entropy oxide/ entropy stabilized oxide as a anode material and also the research has gained immense attention due to high desirable and anticipated values of electrochemical energy storage. Very less excavation in done in the electrolyte spectrum. First started with conductivity which has shown great results that directly started a new era of all solid state storage system. If every aspect of being a ideal electrolyte is sufficed it can be estimated that this new spectrum of material has lot of potential to change the energy storage dynamics of the world .

REFERENCES

1. Berardan D, Sandeep V. Peddada, Robert A. Huggins and Yi Cui : Nano Lett. 2011, 11, 5421–5425
2. Yu Wang and Qianwang Chen : ACS Applied Material and Interfaces 2014 6 6196−6201 3. Feipeng Zhao, Yeyun Wang, Xiaona Xu, Yiling Liu, Rui Song, Guang Lu, and Yanguang Li : ACS App . M t . I t f s 2014 6 11007−11012
4. Peixun Xiong, Guojin Zeng, Lingxing Zeng and Mingdeng Wei : Dalton Trans., 2015, 44, 16746
5. Ali Asghar Ensafi, Najmeh Ahmadi and Behzad Rezaei : RSC Adv., 2015, 5, 91448
6. Yongjin Zou, Qingyong Wang, Cuili Xiang , Zhe She , Hailiang Chu , Shujun Qiu , Fen Xu, Shusheng Liu , Chengying Tang , Lixian Sun : Electrochimica Acta 188 (2016) 126–134
7. Dapeng Zhang, Junshu Zhang, Zengxu Yang, Xiaochuan Ren, Hongzhi Mao, Xianfeng Yang, Jian Yang and Yitai Qian : Chem. Commun., 2017, 53, 10556

8. Ping Nie, Jiaren Yuan, Jie Wang,, Zaiyuan Le, Guiyin Xu, Liang Hao, Gang Pang, Yuting Wu, Hui Dou, Xiaohong Yan and Xiaogang Zhang : ACS Appl. Mater. Interfaces 2017, 9, 20306−20312
9. Jian-Gan Wang, Zhiyong Zhang , Xingrui Liu , Bingqing Wei : Electrochimica Acta 235 (2017) 114–121
10. Lei Zhou, Mingyan Zhang , Yanfang Wang , Yusong Zhu , Lijun Fu, Xiang Liu, Yuping Wu, Wei Huang : Electrochimica Acta 232 (2017) 106–113
11. M. Sookhakian, W.J. Basirun , Mohd Asri Mat Teridi , M.R. Mahmoudian , Majid Azarang , Erfan Zalnezhad , G.H. Yoon , Y. Alias : Electrochimica Acta 230 (2017) 316–323
12. Xiaojuan Zhang , Ping He, Xingquan Zhang , Caixia Li, Huanhuan Liu, Shuai Wang , Faqin Dong : Electrochimica Acta 276 (2018) 92-101
13. Xiaofei Bie , Kei Kubota , Tomooki Hosaka , Kuniko Chihara , Shinichi Komaba : Journal of Power Sources 378 (2018) 322-330
14. Xiaoming Qiu, Yongchang Liu, Luning Wang, Li-Zhen Fan : Applied Surface Science 434 (2018) 1285–1292
15. Anxing Zhou, Liwei Jiang, Jinming Yue, Yuxin Tong, Qiangqiang Zhang, Zejing Lin, Binghang Liu, Chuan Wu, Liumin Suo, Yong-Sheng Hu, Hong Li, and Liquan Chen : ACS App . M t . I t f s 2019 11 41356−41362
16. Samuel Wheeler, Isaac Capone, Sarah Day, Chiu Tang and Mauro Pasta : Chem. Mater. 2019 31 2619−2626
17. Yun Qiu, Ying Lin , Haibo Yang, Lei Wang : Journal of Alloys and Compounds 806 (2019) 1315-1322
18. Xiao Wang, Baoqi Wang, Yuxin Tang, Ben Bin Xu, Chu Liang, Mi Yana and Yinzhu Jiang : J. Mater. Chem. A, 2020, 8, 3222
19. Yun Tang , Wei Li , Pingyuan Feng , Min Zhou , Kangli Wang , Kai Jiang : Chemical Engineering Journal 396 (2020) 125-269
20. Yingbo Yuan, Duan Bin, Xiaoli Dong, Yonggang Wang, Congxiao Wang, and Yongyao Xia : ACS Sust b Ch . E . 2020 8 3655−3663
21. Wei Shi, Pengfei Nie, Guodong Zhu , Bin Hu , Jianmao Yang , Jianyun Liu : Chemical Engineering Journal 388 (2020) 124162
22. Xuezhen Zhu, Haisheng Tao, Maoguo Li : International Journal of Hydrogen Energy 45 (2020) 14452-14460

CHAPTER 3: CHARACTERIZATION TOOLS AND TECHNIQUES

3.1 XRD (X-ray Diffraction)

X-ray diffraction methods are the most effective methods for determining crystal structure of materials including lattice constants and geometry, identification of unknown phases, orientation of single crystals, preferred orientation of polycrystals, defects, stresses etc.

The interaction of the incident monochromatic X-rays with the crystal lattice produces constructive interference when condition satisfy Bragg's law,

$$n\lambda = 2d \sin\theta$$

(3.1)

This law relates the wavelength of X-ray to the diffraction angle (θ) and inter-planar spacing (d) in a crystalline sample. By scanning the sample through a range of 2θ angles, all possible

diffraction peaks to be recorded of the powder sample. Conversion of the diffraction peaks to inter-planar spacing (d) allows identification of the crystalline sample because each of them has a unique d-spacing. Generally, this is achieved by comparison of obtained d-spacings with standard reference patterns (JCPDS, ICDD files etc).

Working Principle :

The basic function of a diffractometer is to detect diffracted X-ray beam from sample and to record the diffraction intensity as a function of the diffraction angle (2θ).Figure 3.1 demonstrates the geometrical arrangement of X-ray diffractometer which consist of three basic elements an X-ray tube, sample holder and an X-ray detector.

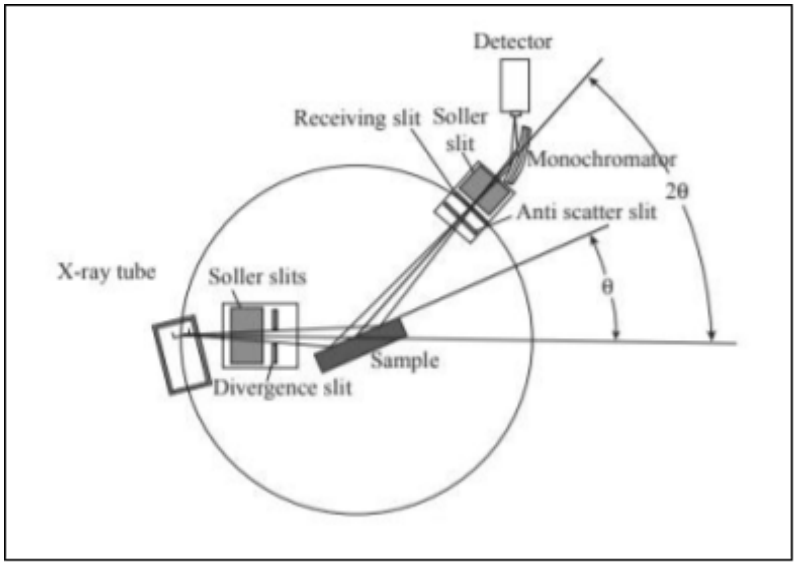

Fig. 3.1 - The geometrical arrangement of X-ray diffractometer

The X-rays are generated by an X-ray tube passes through special slits which collimate the Xray beam. The commonly used Soller slits are made from a set of closely spaced thin metal plates parallel to the figure plane to prevent beam divergence in the direction perpendicular to the figure plane. A divergent X-ray beam passing through the slits strikes the sample. Xrays are diffracted by the sample and form a convergent beam at receiving slits before they enter a detector. The diffracted X-ray beam needs to pass through a crystal monochromator before

being received by a detector. Monochromator is used to eliminate wavelengths other than K_α radiation and also decrease the background radiation originating within the sample. As the sample stage and detector are rotated, the intensity of the reflected X-rays is recorded.

Determination of lattice parameter :

As we know that unit cell of a crystal lattice represented by the a,b,c (length) and α, β, γ (interfacial angles) are known as lattice parameters. Knowing the spacings of crystallographic planes by diffraction method, we can determine the crystal structure of materials.

The inter-planar spacing of cubic crystal relates to the lattice parameter (a) by the following equation,

$$d_{hkl} = \frac{a}{\sqrt{h^2+k^2+l^2}} \quad (3.2)$$

Where 'd_{hkl}' is the inter-planar distance, 'a' is the lattice parameter, 'h', 'k', 'l' is known as Miller indices.

Determination of the crystallite size :

In reality, diffraction from a crystalline sample produces a peak with a certain width. The peak width can result from the size effect of the crystals and strain etc.

The average crystallite size can be calculated according to Debye-Scherrer's equation

$$D = \frac{0.9\lambda}{\beta \cos\theta} \quad (3.3)$$

Where D is average crystallite size, β corresponds to line broadening in radians (FWHM), θ is the Bragg angle, λ is X-ray wavelength (0.154 nm).

Basically, Peak width is inversely related to crystal size that means peak width increases with decreasing crystal size.

3.2. FESEM (Field Emission Scanning Electron Microscopy)

The field emission scanning electron microscopy (FESEM) is the most widely used technique to visualize very small topographical details by scanning the sample surface. It also examines morphology and microstructure of bulk and nanomaterials and devices.

Working Principle :

A scanning electron microscope consists of an electron gun and a series of electromagnetic lenses, apertures, scanning coils and detectors as shown in Fig. 3.2.

A typical FESEM systems use a field emission electron gun for generating an electron beam. The acceleration voltage for generating an electron beam is typically $\sim$30 kV.

The optical path goes through several electromagnetic lenses, including condenser lenses and one objective lens in a FESEM system. The electromagnetic lenses are for electron probe formation. The two condenser lenses reduce the crossover diameter of the electron beam and the objective lens focuses the electron beam as a probe with a diameter of 1-10 nm.

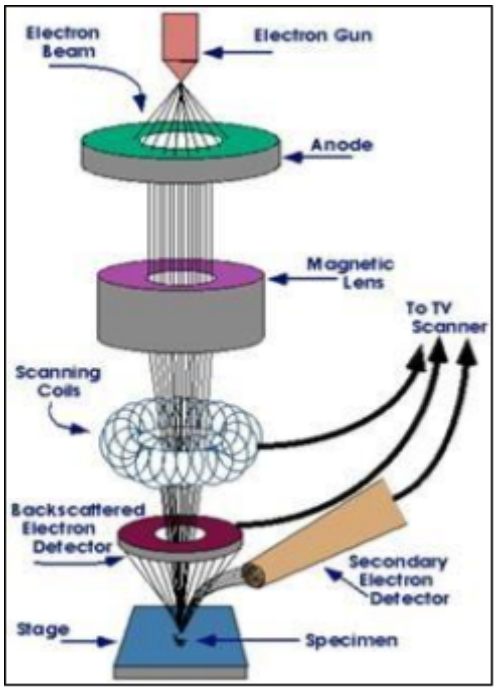

Fig. 3.2 - Schematic diagram of FESEM

Probe scanning is operated by a beam deflection system which is controlled by two pairs of electromagnetic coils. The first pair of scan coils bends the beam off the optical axis of the microscope and the second pair of scan coils bends the beam back onto the axis at the pivot point of a scan. The apertures are mainly used for limiting the divergence of the electron beam in its optical path.

The deflection system moves the probe over the sample surface along a straight line and then displaces the probe to a position on the next line for scanning, so that a rectangular raster is generated on the sample surface. The signal from emitted electrons are collected by a detector for imaging purpose.

Digital imaging generates an image by averaging multiple scans for the same area which helps to reduce the background noise in imaging.

The magnification of an FESEM is determined by the ratio of the linear size of the display screen to the linear size of the specimen area being scanned. The size of the scanned rectangular area can be varied over a wide range.

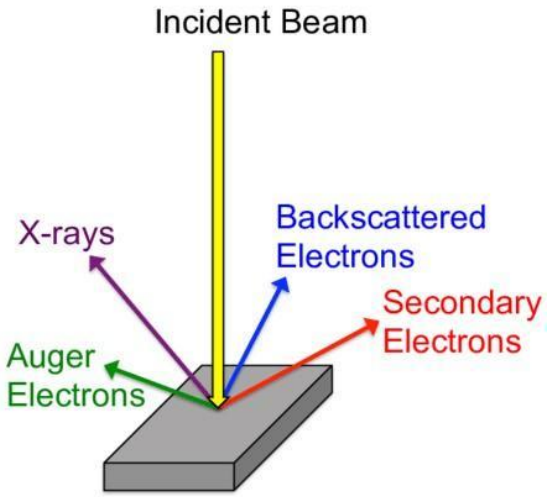

Fig. 3.3 – Electron-sample interaction and type of signal generated

To understand signal detection, knowledge of electron signal types that are useful in FESEM is necessary : backscattered electrons and secondary electrons. When highly energized electrons impart onto a sample, they produce either elastic or inelastic scattering. Elastic scattering produces the backscattered electrons (BSEs) and inelastic scattering produces secondary electrons (SEs). BSEs are typically deflected from the sample surface at large angles and essentially possess the same energy as the incident electrons. However, SEs are typically deflected at small angles and show considerably low energy compared with incident electrons. Inelastic scattering knock off electrons from the atoms constituting the sample itself, these are known as secondary electrons.

SEs are useful for achieving topographic contrast and BSEs are useful for formation of elemental composition contrast. Additionally X-ray mapping can also be observed which have been used for chemical characterization.

3.3. FTIR (Fourier Transform Infrared Spectroscopy)

Fourier transform infrared spectroscopy is a technique to analyse the structure of molecules by examining the interaction between IR radiation and vibrations in molecules. When a molecule is irradiated by electromagnetic waves within the infrared frequency range, one

particular frequency may absorbs the vibrational frequency of the molecule. These absorption frequencies represent the excitation of vibrations of chemical bonds, and thus specifies the type of the bond and the functional groups that are present in a molecule.

In Fourier transform infrared (FTIR) spectroscopy experiment, the intensity of a beam of IR radiation is measured after it interacts with the sample as a function of light frequency which is subjected to Fourier transform to convert infrared spectrum (intensity vs frequency) to intensity-time output. The identity of a pure compound or to detect the presence of specific impurities, atomic arrangement and concentrations of the chemical bonds that are present in the sample can be determined.

Working Principle :

The schematic diagram of an FTIR spectrophotometer is shown in Fig. 3.4. The basic components of FTIR spectrophotometer are Light Source (IR), Interferometer, sample holder, a detector, signal processor and readout.

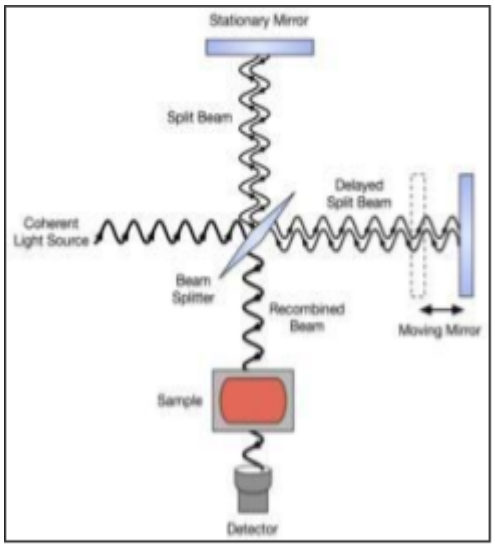

Fig. 3.4 - Schematic diagram of FTIR spectrophotometer

1. **The source :** Infrared energy is emitted from a black body source. Commonly used sources are Globar filament and Nernst glower.

2. **The interferometer :** The beam of radiation enters the interferometer where the "spectral encoding" occurs.

Interferometer employs a beam splitter which divides the incoming infrared beam into two optical beams. One beam reflects off of a mirror which is fixed in position and the other beam reflects off of a moving mirror. The two beams reflect off of their respective mirrors and are

recombined to a single beam when they return at the beam splitter. Depending on the relative path lengths, these two beams interfere with each other.

The interferometer produces interferogram signal which include all of the infrared frequencies "encoded" into it.

3. **The sample :** The beam enters the sample chamber where it is transmitted through or reflected from the sample surface, depending on the type of analysis being performed. This is where specific vibrational frequencies which are uniquely characteristic of the sample, are absorbed.

4. **The detector :** The beam passes to the detector for final measurement. The detector measures the interferogram signal.

5. **The computer :** The digitized signal is sent to the computer to carry out Fourier transformation. Finally the sample infrared spectrum is presented to the user for interpretation.

3.4. UV-Visible Spectroscopy

Ultraviolet−Visible spectroscopy is a widely used analytical method for the quantitative and qualitative characterization of nanomaterials and nanostructures. This method is important to

both determine the concentration and study the electronic structure. UV-Visible spectral study is also used to determine the optical band gap.

The basic principle of quantitative UV-Vis spectroscopy lies in comparing the extent of absorption of a sample solution with that of a set of standards under radiation of selected wavelength through the application of Beer-Lambert law. The Beer-Lambert law states that the absorbance of a solution is directly proportional to the concentration of the absorbing species in the solution and the path length.

According to Beer-Lambert's law,

$$A = log_{10}\left(\frac{I_0}{I}\right) = \varepsilon c l \quad (3.4)$$

Where, A is measured absorbance, I_0 is the intensity of light passing through reference cell, I is the intensity of light passing through sample cell, ε is the molar extinction coefficient, c is the concentration of the light absorbing substance and l is the path length of the sample.

Extinction coefficient or the integral absorption over an absorption band gives the magnitude of the transition dipole moment and are also dependent on geometry and molecular structure.

Working Principle :

UV-Visible spectrophotometers consist of a number of fundamental components : Light Sources (UV and VIS), monochromator, sample holder, a detector, signal processor and readout. The radiation source used is often a tungsten filament, a deuterium arc lamp which is continuous over the ultraviolet region, and more recently xenon arc lamps for the visible wavelengths. The commonly used detector is a photodiode or a charge coupled device (CCD). Photodiodes are used with monochromators, so that only light of a single wavelength reaches the detector. When measuring absorbance at the particular region, the other lamp has to be turned off. Fig. 3.5 shows schematic diagram of UV−Vis Spectrophotometer.

The light source is a monochromator which splits the incident beam of light into two equal intensity beams (sample and reference beam) by a half mirrored device before it reaches the sample. The sample beam, passes through a cuvette containing a solution of the compound being studied in a transparent solvent and the reference beam, passes through an identical cuvette containing only the solvent. Quartz or fused silica cuvettes are required for UV−Vis spectroscopy.

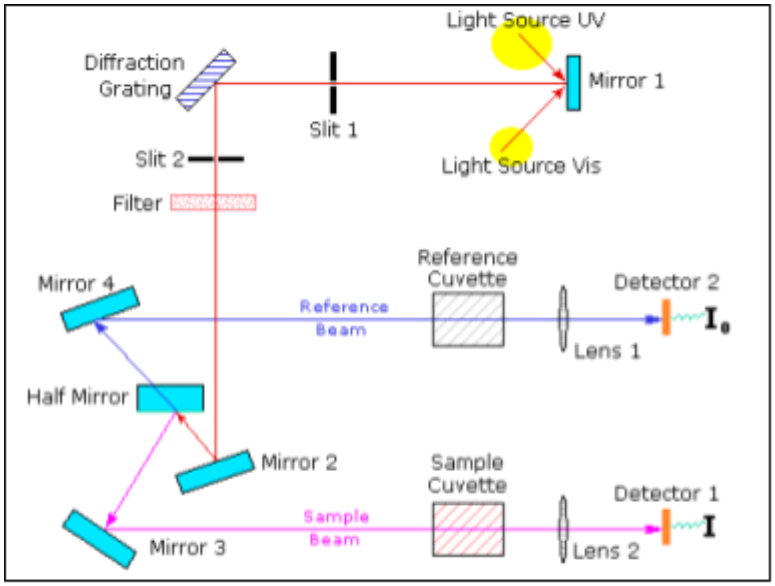

Fig. 3.5 - Schematic diagram of UV–Vis Spectrophotometer

The light sensitive detector measures the intensity of light transmitted from the cuvettes and passes the information to a meter that records and displays the value to the operator on an LCD screen. The sample beam and reference beam both are measured at the same time. The intensity of the sample beam is defined as I and the intensity of the reference beam is defined as I_0. Over a short period of time, the Spectrometer automatically scans all the component wavelengths in the manner described. The ultraviolet (UV) region scanned is normally from 200 to 400 nm, and the visible region is from 400 to 800 nm. A complete spectrum of the absorption at all wavelengths is recorded.

Band gap determination :

Using the recorded data of absorption spectrum in the whole range of wavelength, we can calculate the absorption coefficient (α) of the material.

The relation between absorption coefficient and photon energy was deduced by Tauc and is represented as,

$$(\alpha h\nu)^{1/n} = A\left(h\nu - E_g\right)$$

(4.2)

Where α is the absorption coefficient, n assumes values like 2 and 1/2 in accordance with indirect and direct allowed transitions and , $h\nu$ is photon energy, E_g is band gap and A is proportionality constant.

According to equation (4.2), the plot of $(\alpha h\nu)^{1/n}$ versus $h\nu$ must be a straight line and from its intercept on the $h\nu$ axis, band gap of the material can be determined.

REFERENCES

1. Handbook of Nanotechnology : Bharat Bhushan, Springer, 2004
2. Fundamentals Of Nanoelectronics : George W. Hanson , Pearson Education, 2009
3. Nanostructure and nanomaterials synthesis, properties & applications : Guozhong Cao, Imperial College Press, 2004
4. Introduction to Nano; Basic to Nanoscience and Nanotechnology : Amretashis Sengupta, Chandan Kumar Sarkar, Springer, 2015
5. Materials Characterization; Introduction to Microscopic and Spectroscopic Methods : Yang Leng, John Wiley & Sons , 2008
6. Introduction to Solid State Physics : Charles Kittel, , John Wiley & Sons, 7th edition
7. Elements of X-ray Diffraction : B. D. Cullity, Addison-Wesley Publishing Company, inc
8. Crystal Structure Determination : Werner Massa, Springer, 2nd edition
9. Fundamentals of Molecular Spectroscopy : Colin N. Banwell and Elaine M. McCash, McGraw Hill Education, 4th edition

CHAPTER 4: SYNTHESIS AND CHARACTERIZATION OF $(MgNiCuCoZn)_{1-x}Li_xO$ AND ITS ANALOGUES

4.1. Detailed Synthesis Procedure

Chemicals :

Analytical graded Magnesium nitrate[$Mg(NO_3)_2.6H_2O$; Merck Chemicals] , Copper Nitrate [$Cu(NO_3)_2.3H_2O$; Merck Chemicals] , Nickel nitrate [$Ni(NO_3)_2.6H_2O$; Merck Chemicals] , Cobalt nitrate [$Co(NO_3)_2.6H_2O$; Merck Chemicals] , Zinc Nitrate [$Zn(NO_3)_2.6H_2O$; Merck Chemicals] , Potassium carbonate [K_2CO_3 ; Merck Chemicals], Lithium Nitrate [$LiNO_3.H_20$; Merck chemicals] , Ethanol [Merck Chemicals] and deionized water (DW) were used for this experiment.

Synthesis of (MgNiCuCoZn)O :

1. The proper amount of salts was dissolved in de-ionized water to obtain a first solution (A) with 0.1 M total cationic concentration (0.02 M for each cation) . Here salts were taken dissolve in 80ml DI.

$Mg(NO_3)_2.6H_2O$ – 410.256 mg

$Cu(NO_3)_2.3H_2O$ – 386.56 mg

$Ni(NO_3)_2.6H_2O$ – 465.264 mg

$Co(NO_3)_2.6H_2O$ – 473.0368 mg

$Zn(NO_3)_2.6H_2O$ – 475.984 mg

Stirring was carried out for about 45min to form an homogenous mixture.

2. K_2CO_3 was dissolved in de-ionized water to form 0.15 M solution (B). Here salt was taken For 80ml DI.

K_2CO_3 – 1660 mg

3. The co-precipitation was carried out in reverse mode, i.e., by slowly adding solution A to solution B drop wise, under vigorous stirring.

4. The mix was kept under continuous stirring for 45 min and, finally, the gelatinous co-precipitate was obtained of olive green colour with pH - 9,

5.The the entire sample was repeatedly washed with de-ionized water and centrifuged at 4500 rpm and then the precipitated sample was mixed with ethanol and dried overnight at 60°C and collected a olive green sample.

6. Then the powder was pelletized with approx. 1.4 – 1.6gm and was sintered with 1100°C for 15h and air-quenched immediately. This is classified as **Li0**.

Synthesis of $(MgNiCuCoZn)_{0.95}Li_{0.05}O$:

1. The proper amount of salts was dissolved in de-ionized water to obtain a first solution (A) with 0.1 M total cationic concentration (0.02 M for each cation) . Here salts were taken dissolve in 80ml DI.

$Mg(NO_3)_2.6H_2O$ – 410.256 mg

$Cu(NO_3)_2.3H_2O$ – 386.56 mg

$Ni(NO_3)_2.6H_2O$ – 465.264 mg

$Co(NO_3)_2.6H_2O$ – 473.0368 mg

$Zn(NO_3)_2.6H_2O$ – 475.984 mg

$Li(NO)_3.H_2O$ – 52.4mg

Stirring was carried out for about 45min to form an homogenous mixture.

2. K_2CO_3 was dissolved in de-ionized water to form 0.15 M solution (B). Here salt was taken For 80ml DI.

K_2CO_3 – 1660 mg

3. The co-precipitation was carried out in reverse mode, i.e., by slowly adding solution A to solution B drop wise, under vigorous stirring.

4. The mix was kept under continuous stirring for 45 min and, finally, the gelatinous co-precipitate was obtained of olive green colour with pH - 9,

5.The the entire sample was repeatedly washed with de-ionized water and centrifuged at 4500 rpm and then the precipitated sample was mixed with ethanol and dried overnight at 60°C and collected. collected a olive green sample.

6. Then the powder was pelletized with approx. 1.4 – 1.6gm and was sintered with 1100°C for 15h and air-quenched immediately. This is classified as **Li5**

Synthesis of $(MgNiCuCoZn)_{0.925}Li_{0.075}O$:

1. The proper amount of salts was dissolved in de-ionized water to obtain a first solution (A) with 0.1 M total cationic concentration (0.02 M for each cation) . Here salts were taken dissolve in 80ml DI.

$Mg(NO_3)_2.6H_2O$ – 410.256 mg

$Cu(NO_3)_2.3H_2O$ – 386.56 mg

$Ni(NO_3)_2.6H_2O$ – 465.264 mg

$Co(NO_3)_2.6H_2O$ – 473.0368 mg

$Zn(NO_3)_2.6H_2O$ – 475.984 mg

$Li(NO)_3.H_2O$ – 78.6mg

Stirring was carried out for about 45min to form an homogenous mixture.

2. K_2CO_3 was dissolved in de-ionized water to form 0.15 M solution (B). Here salt was taken For 80ml DI.

K_2CO_3 – 1660 mg

3. The co-precipitation was carried out in reverse mode, i.e., by slowly adding solution A to solution B drop wise, under vigorous stirring.

4. The mix was kept under continuous stirring for 45 min and, finally, the gelatinous co-precipitate was obtained of olive green colour with pH - 9,

5.The the entire sample was repeatedly washed with de-ionized water and centrifuged at 4500 rpm and then the precipitated sample was mixed with ethanol and dried overnight at 60°C and collected. collected a olive green sample.

6. Then the powder was pelletized with approx. 1.4 – 1.6gm and was sintered with 1100°C for 15h and air-quenched immediately. This is classified as **Li7**

Synthesis of $(MgNiCuCoZn)_{0.90}Li_{0.10}O$:

1. The proper amount of salts was dissolved in de-ionized water to obtain a first solution (A) with 0.1 M total cationic concentration (0.02 M for each cation) . Here salts were taken dissolve in 80ml DI.

$Mg(NO_3)_2.6H_2O$ – 410.256 mg

$Cu(NO_3)_2.3H_2O$ – 386.56 mg

$Ni(NO_3)_2.6H_2O$ – 465.264 mg

$Co(NO_3)_2.6H_2O$ – 473.0368 mg

$Zn(NO_3)_2.6H_2O$ – 475.984 mg

$Li(NO)_3.H_2O$ – 104.8mg

Stirring was carried out for about 45min to form an homogenous mixture.

2. K_2CO_3 was dissolved in de-ionized water to form 0.15 M solution (B). Here salt was taken For 80ml DI.

K_2CO_3 – 1660 mg

3. The co-precipitation was carried out in reverse mode, i.e., by slowly adding solution A to solution B drop wise, under vigorous stirring.

4. The mix was kept under continuous stirring for 45 min and, finally, the gelatinous co-precipitate was obtained of olive green colour with pH - 9,

5.The the entire sample was repeatedly washed with de-ionized water and centrifuged at 4500 rpm and then the precipitated sample was mixed with ethanol and dried overnight at 60°C and collected a olive green sample.

6. Then the powder was pelletized with approx. 1.4 – 1.6gm and was sintered with 1100°C for 15h and air-quenched immediately.This is classified as **Li10**

4.2. Characterization of Prepared Samples

The as-synthesized samples were characterized by X-ray diffraction (XRD, Rigaku Ultima III) using Cu-K_α radiation of wavelength λ = 1.54 Å for the structural information. Identification of the phases were done with the help of the Joint Committee on Powder Diffraction Standards (JCPDS) files. The Fourier transformed infrared spectra were recorded on a Shimadzu-8400S FTIR spectrometer using KBr pellets method. The DRS spectra was also recorded with Ba_2SO_4 integrating sphere .

4.2.1. XRD Analysis

The crystal structure of the as-synthesized (MgNICuZnCo)O and its Lithium analogues was analyzed by X-ray diffraction (XRD), shown in Fig. 4.2. The prepared samples Li0, Li5, Li7, Li10 were scanned in 2θ mode from 30°– 80°.

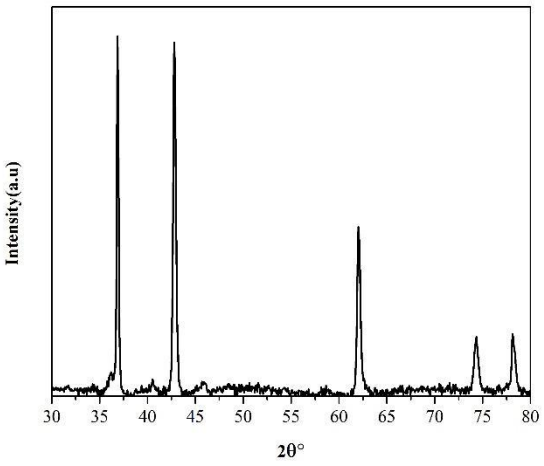

Fig. 4.2a - XRD pattern of synthesized sample Li0

The four highly intense diffraction peaks at 2θ = 36.87º, 42.79º, 62.02º, 74.36º and 78.13º corresponds to the ( ), ( ), ( ), ( ) and ( ) planes of Li0. All reflections can be well indexed into face centered cubic (MgNiCoZnCu)O with a space group of Fm3m. The lattice constant obtained is **a=b=c=4.212 A° and α=ß=ɣ=90°**, which agrees well with the existing JCPDS card no. 780430. There is no evidence in the XRD pattern for the presence of other phase or impurities in Li0 sample (Fig. 4.2.a).

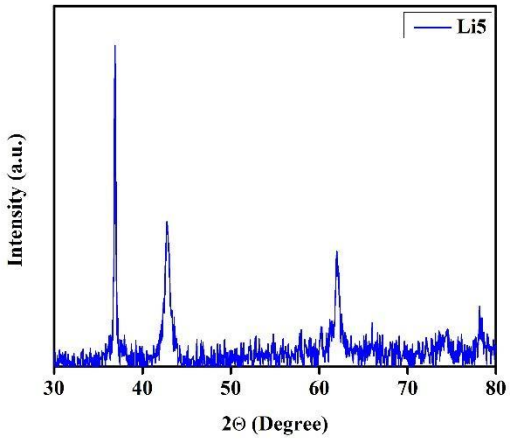

Fig. 4.2 b- XRD pattern of synthesized sample Li5

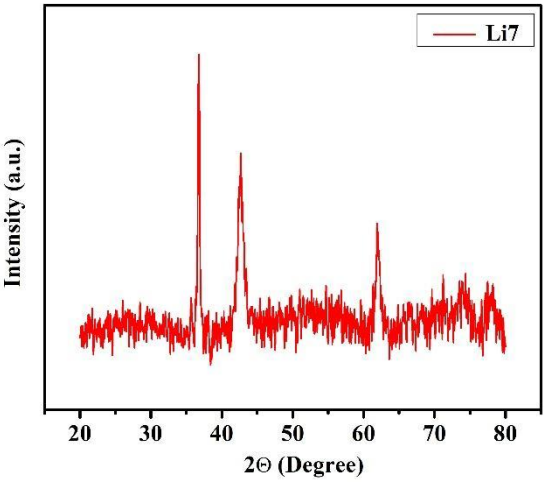

Fig. 4.2 c - XRD pattern of synthesized sample Li7

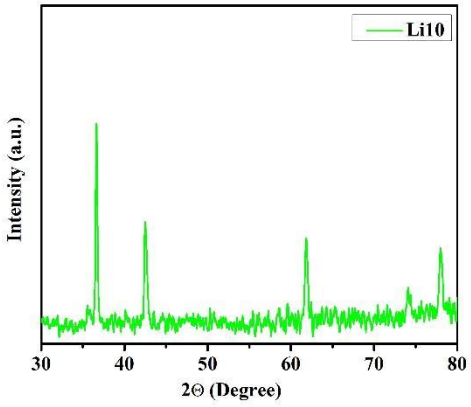

Fig. 4.2 d- XRD pattern of synthesized sample Li10

The XRD pattern of the sample Li5, Li7 and Li10 are shown in the Fig. 4.2 (b),(c),(d) respectively. The three highly intense diffraction peaks at 2θ = 36.89º, 42.85º, 62.02º and low

intensity peaks at 74.68º and 78.30º corresponds to the (1 1 1), (2 0 0) and (2 2 0) planes and (3 1 1) and (2 2 2) planes of Li0. The three highly intense diffraction peaks at 2θ = 36.82º, 42.85º, 62.40º and corresponds to the (1 1 1), (2 0 0) and (2 2 0) planes of Li7. The three highly intense diffraction peaks at 2θ = 36.74º, 42.36º, 62.82º corresponds to the (1 1 1), (2 0 0) and (2 2 0) planes of Li10. With increase in the lithium amount the intensity of peaks has reduced slightly above 70°.

The XRD pattern for each sample shows corresponding sets of peaks characteristic $(MgNiCuZnCo)_{1-x}Li_xO$ like face centered cubic lattices. The required is a single phase rocksalt structure and that is what received in every sample powder XRD corresponding to MgO data of JCPDS.

The average crystallite size is calculated according to Debye-Scherrer's equation

$$D = \frac{0.9\lambda}{\beta \cos\theta} \tag{4.1}$$

Where, D is average crystallite size, β corresponds to full width at half maxima (FWHM) of the diffraction pattern, θ is Bragg angle, λ is X-ray wavelength (0.154 nm).

Sample code	**Average crystallite size(D) (nm)**
Li0	24.801
Li5	21.510
Li7	18.927
Li10	16.550

Table 1 - Average crystallite size of synthesized samples Li0, Li5, Li7, Li10

4.2.2. FTIR Spectra Analysis

FTIR spectrum was recorded to understand the chemical bonding and molecular structure of Li0, Li5, Li7 and Li10 sample shown in Fig.4.5.

According to the group factor analysis theory, a rocksalt lattice with O^5_h symmetry has two F_{1U} IR active modes. The rocksalt lattice has 4 equivalents points for the cation and the anion with each set of equivalents points giving rise to F_{1U} peaks, one being acoustic and the other optical. The FTIR spectra of Li0,Li5,Li7,Li10 are shown in Fig. 4.5. The observed broadening of the peaks at 469 cm^{-1}, 496 cm^{-1} , 505 cm^{-1} and 514 cm^{-1} for Li0, Li5, Li7, Li10 respectively were attributed to the presence of different cations in the lattice as each would result in a different relaxation behaviour. When the structure symmetry is preserved, the peaks produced would be extremely close, but even a little shift would result in a broadened peak, as is observed when substitutional doping is done in the lattice. Pure Li_2O exhibits a peak at 1110 cm^{-1} which was not observed in the FTIR spectra, hence ruling out the possibility of Li_2O being present as a minor second phase and confirming that the synthesised compound was phase-pure rocksalt.

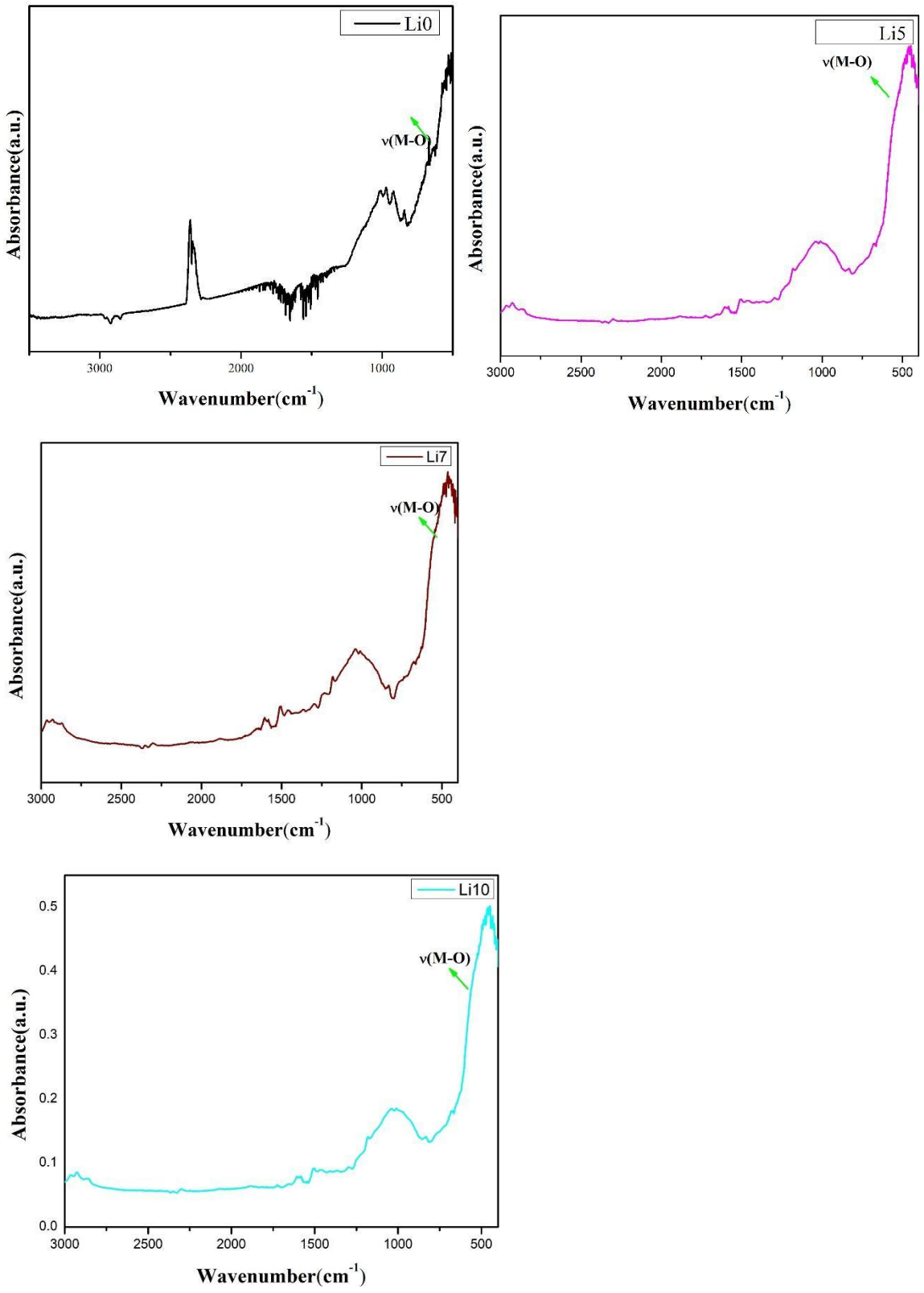

Fig. 4.5 - FTIR spectra of synthesized samples Li0, Li5, Li7, Li10

4.2.4. UV- Visible DRS Spectra Analysis

Ultraviolet−Visible DRS spectral study was recorded to understand the electronic structure and the optical band gap of Li0, Li5, Li7 and Li10 sample shown in Fig.4.6.

Obtained band gap (E_g) of Li0 from Tauc plot is 0.129eV (Fig.4.7.a).

The relation between absorption coefficient (α) and photon energy $(h\nu)$ was deduced by Tauc and is represented as,

$$(\alpha h\nu)^{1/n} = A\left(h\nu - E_g\right) \quad (4.2)$$

Where α is the absorption coefficient, $n = \frac{1}{2}$ for direct allowed transitions, $h\nu$ is photon energy, E_g is band gap and A is proportionality constant. Using equation (4.2) band gap of the prepared samples can be calculated.

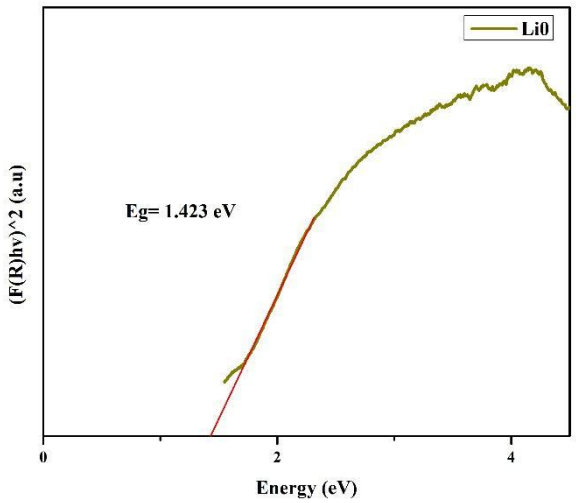

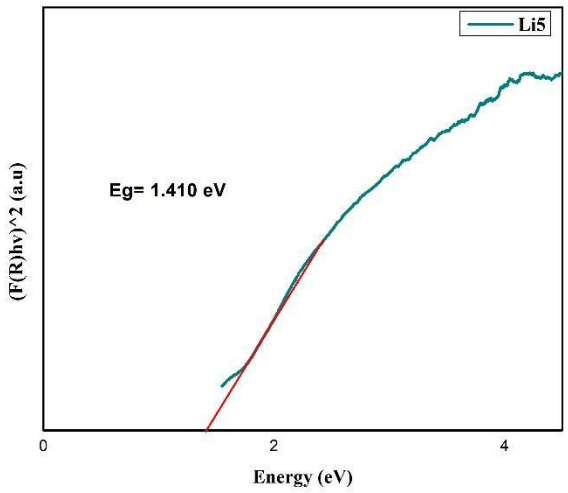

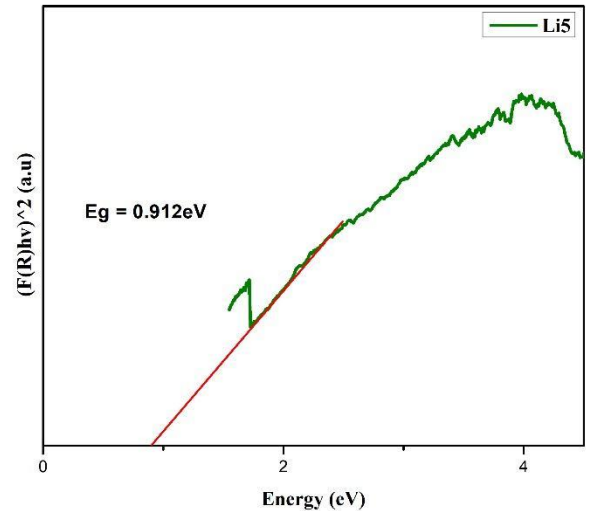

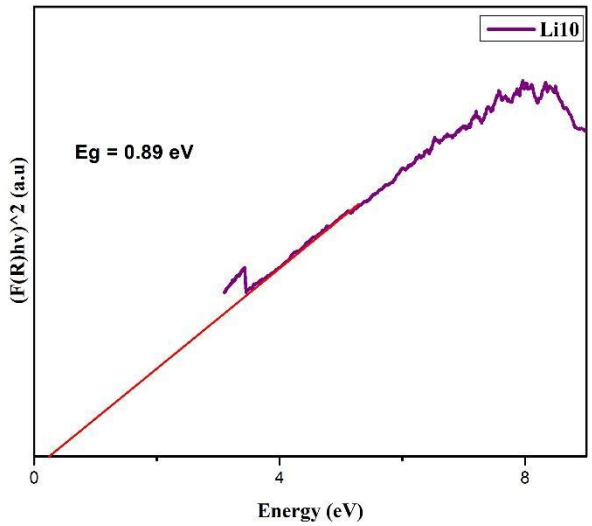

Fig. 4.6 - Tauc plot of samples a) Li0, b) Li5, c)Li7, d)Li10

Obtained band gap (E_g) of Li0, Li5 from Tauc plot is 1.423 eV and 1.410 eV respectively and E_g of Li7 and Li10 is 0.912 eV and 0.89 eV ……(Fig.4.6).

For all HEOx samples the resistance changes in an exponential manner as in a semiconductor with electrical band-gaps of about ~1.5 eV, gap that decreases with Li substitution. This band gap can be correlated to the absorption mechanism that can be observed in the UV-Vis absorption spectra. When undoped the band gap is very less. As soon as Lithium came into the scenario there is huge change in the band gap also with increase in lithium percentage the band gap considerably decreases. Hence we can assume that more the doping or moving charge for transportation lesser the band gap.

REFERENCES

1. Kaiqiang Zhang, Tae Hyung Lee, Hyunho Noh, Omar K. Farha,, Ho Won Jang, Ji-Won Choi and Mohammadreza Sh uh h : : C yst. wth D s. 2019 19 7385−7395
2. Mohammadreza Shokouhimehr, Eric S. Soehnlen, Anatoly Khitrin , Soumitra Basu, Songping D. Huang : Inorganic Chemistry Communications 13 (2010) 58–61
3. Colin D. Wessells, Sandeep V. Peddada, Robert A. Huggins and Yi Cui : Nano Lett. 2011, 11, 5421–5425
4. u W d Q w Ch : ACS App d M t d I t f s 2014 6 6196−6201 5. Feipeng Zhao, Yeyun Wang, Xiaona Xu, Yiling Liu, Rui Song, Guang Lu, and Yanguang Li : ACS Appl. Mater. Interfaces 2014, 6, 11007−11012
6. Dezhi Yang, Jing Xu, Xiao-Zhen Liao, Yu-Shi He, Haimei Liu and Zi-Feng Ma : Chem. Commun., 2014, 50, 13377
7. Peixun Xiong, Guojin Zeng, Lingxing Zeng and Mingdeng Wei : Dalton Trans., 2015, 44, 16746

8. Dapeng Zhang, Junshu Zhang, Zengxu Yang, Xiaochuan Ren, Hongzhi Mao, Xianfeng Yang, Jian Yang and Yitai Qian : Chem. Commun., 2017, 53, 10556
9. Ping Nie, Jiaren Yuan, Jie Wang,, Zaiyuan Le, Guiyin Xu, Liang Hao, Gang Pang, Yuting Wu, Hui Dou, Xiaohong Yan and Xiaogang Zhang : ACS Appl. Mater. Interfaces 2017, 9, 20306−20312
10. Xiaojuan Zhang , Ping He, Xingquan Zhang , Caixia Li, Huanhuan Liu, Shuai Wang , Faqin Dong : Electrochimica Acta 276 (2018) 92-101
11. Xiaofei Bie , Kei Kubota , Tomooki Hosaka , Kuniko Chihara , Shinichi Komaba : Journal of Power Sources 378 (2018) 322-330
12. Xiao Wang, Baoqi Wang, Yuxin Tang, Ben Bin Xu, Chu Liang, Mi Yana and Yinzhu Jiang : J. Mater. Chem. A, 2020, 8, 3222
13. Anxing Zhou, Liwei Jiang, Jinming Yue, Yuxin Tong, Qiangqiang Zhang, Zejing Lin, Binghang Liu, Chuan Wu, Liumin Suo, Yong-Sheng Hu, Hong Li, and Liquan Chen : ACS App . M t . I t f s 2019 11 41356−41362
14. Samuel Wheeler, Isaac Capone, Sarah Day, Chiu Tang and Mauro Pasta : Chem. Mater. 2019 31 2619−2626
15. Samik Saha, Atanu Roy , Apurba Ray , Trisha Das , Mahasweta Nandi , Basudev Ghosh , Sachindranath Das : ElectrochImica Acta 353(2020) 136515
16. Yun Tang , Wei Li , Pingyuan Feng , Min Zhou , Kangli Wang , Kai Jiang : Chemical Engineering Journal 396 (2020) 125-269
17. Yingbo Yuan, Duan Bin, Xiaoli Dong, Yonggang Wang, Congxiao Wang, and Yongyao Xia : ACS Sust b Ch . E . 2020 8 3655−3663

CHAPTER 5: STUDY OF DIELECTRIC PROPERTIES OF (MgNiCuZnCo)O AND ITS LITHIUM ANALOGUES

5.1. Dielectric Sample Preparation

Samples used for measurements were as obtained bars, thinned to about 2 mm, and with a surface of about 20 mm2 to 30 mm2 . The large parallel faces were painted with silver paste for making electrical contacts. The contact resistance was of the order of a few Ohm, several orders of magnitude smaller than the resistance exhibited by the samples.

Scan impedance analysis was performed with a HIOKI impedance meter , by scanning samples from 3 MHz to 4 Hz with 30 measurements per log value and applying an AC signal amplitude of 1 V peak to peak.

5.2. Dielectric spectroscopy Study of as-Synthesized Samples

5.2.1 Frequency dependence. The dielectric spectroscopic study provides insights into the structure of compounds, grain boundary, grain, transport properties and charge storage capabilities of dielectric material. The dielectric properties depend on several factors, including the chemical composition and the method of preparation.

The frequency dependence of the real part (ε') of permittivity of HEOLi$_x$ (x = 0.00, 0.05 and 0.075) at different temperatures is shown in below figures. The dielectric constant (ε') decreased rapidly with the increase in frequency. This decrease is due to the reduction of space charge polarization effect. Then, it remained nearly constant but, increased with increasing temperature at a given frequency. However, at low frequency the dielectric constant was high. This is due to the presence of space charge polarization at the grain boundaries, which generates a potential barrier. Then, an accumulation of charge at the grain boundary occurred, which led to higher values of the real part of permittivity. The dielectric dispersion can be explained by the dominance of grain boundaries' effect rather than by the grains. This is attributed to Maxwell–Wagner type of interfacial polarization in accordance with Koop's phenomenological theory.

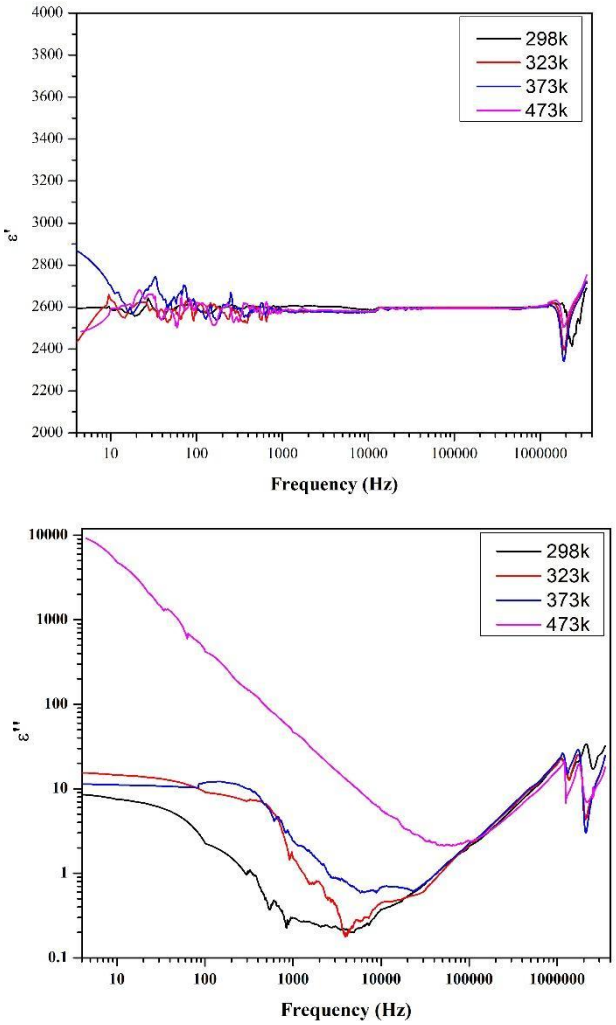

Fig. 5.1a - Frequency dependence of Real and imaginary permittivity of Li0

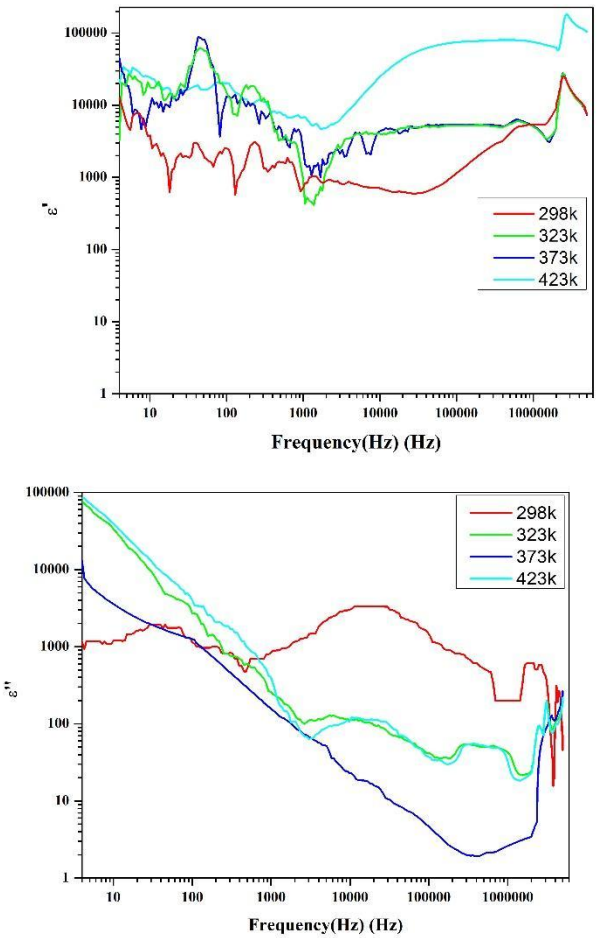

Fig. 5.1b - Frequency dependence of Real and imaginary permittivity of Li5

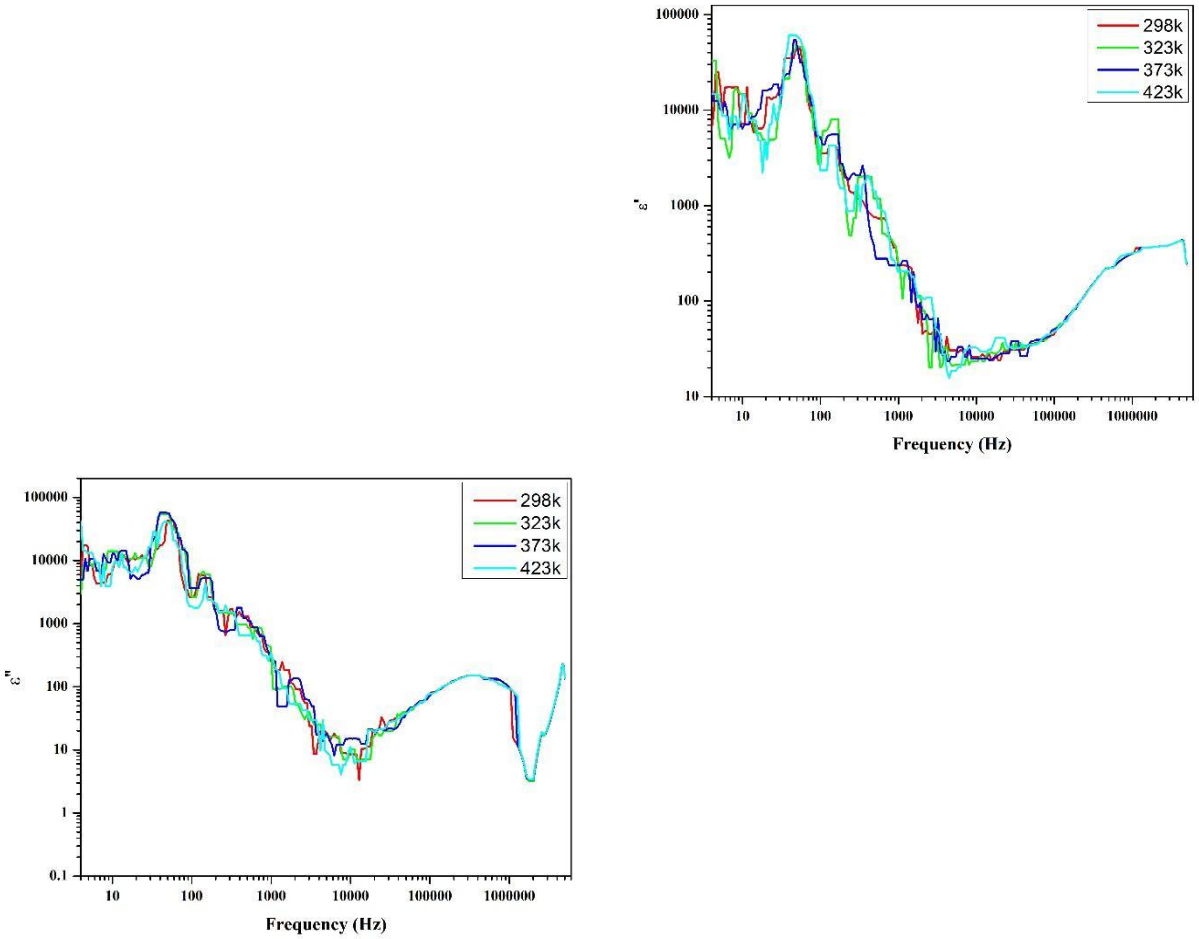

Fig. 5.1c - Frequency dependence of Real and imaginary permittivity of Li7

The relative permittivity (ε) is very large for all samples with no maximum observed in the temperature range of the measurement. The relative permittivity at 423K measured at 71.23 Hz with a EIS meter is close to 1×10^5 for HEOx-Li7 , making these samples **colossal dielectric constant (CDC) materials**.

The dielectric loss tangent, tan(δ), is related to the dielectric relaxation process and is given as the ratio of the imaginary part ε'' and the real part ε', *i.e.*, $\tan(\delta) = \varepsilon''/\varepsilon'$. The dielectric loss represents the energy loss and occurs when the polarization shifts behind the applied electric field caused by the grain boundaries.

In general, the dielectric loss of dielectric materials originates from three distinct factors: space charge migration (interfacial polarization contribution), direct current (DC) conduction, and movement of the molecular dipoles (dipole loss).

To explain the decrease of the real part of permittivity at higher frequencies, we supposed that the dielectric structure is composed of low resistive grains separated by poor conducting thin grain boundaries. As a result of the applied electric field, we obtained a localized accumulation of charges, which led to the interfacial polarization.

The frequency dependence of the dielectric loss tangent at different temperatures is shown in below figure. The curve shows the same behaviour of the dielectric constant (ε'). The high value of tan(δ) at a low frequency can be attributed to the high resistivity of grain boundaries which are more effective than the grains.

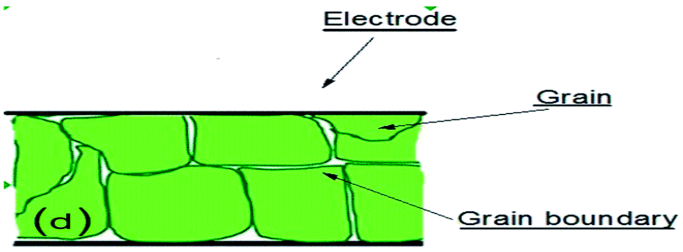

Fig. 5.2 – Grain and Grain Boundary of pellet and electroding

Grain and grain boundary play a vital role, lesser the gaps within the grain boundary better is the structure and density. As per literature, the diameter also has an important attention. As per study, the dielectric losses remain constant whatever the diameter value. Density measurements have been performed on each sample and values are nearly the same for each of these pellets of different diameters, showing that sample densification is not responsible for the observed differences. One obvious factor that may influence the changes in the material permittivity with the electrode diameter is a different grain size. Spectroscopy observations conducted on a 9.98-mm diameter sample (Li0) did show significant differences in grain size compared to a 6.74 mm(Li5) and 6.41 mm(Li7) diameter pellet.

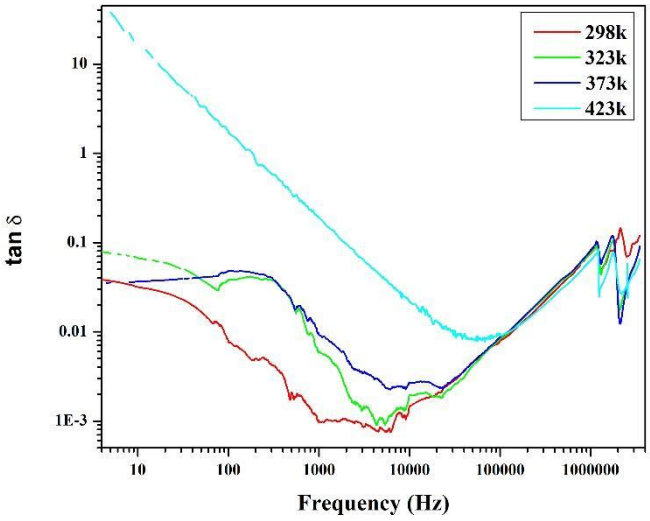

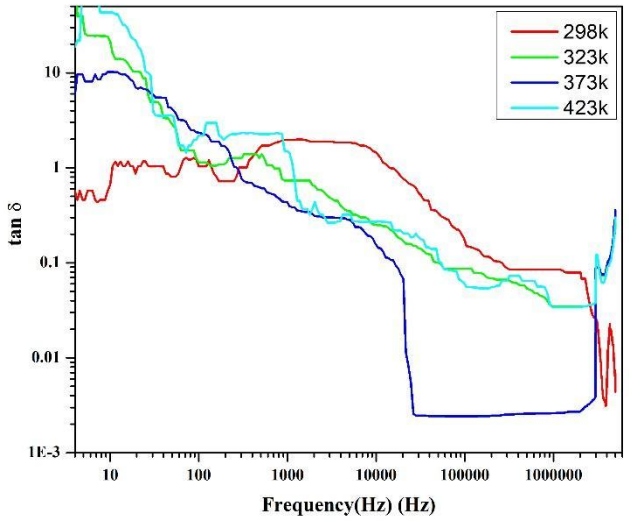

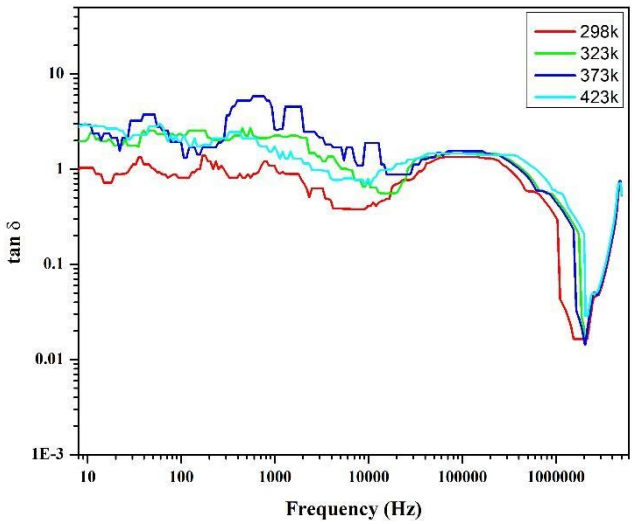

Fig. 5.3 - Frequency dependence of loss factor of Li0, Li5 and Li7

All the above data indicate that Li-doping influences the variation of temperature. It also can be seen that ε_{max} decreases with the increase of Li concentration. Literature proposes that ε_{max} strongly depends upon the size of the grains.

In fact, the dielectric constant of the materials is linearly proportional to the average value of grain size. Therefore, the decrease of dielectric constant and loss tangent as a function of Co doping is due to the decrease of grain size, which is in agreement with the previous results (conduction mechanism). This indicates that there is a strong relation between the conduction process and the dielectric polarization in these Li doped HEO. In addition, Percentage of Lithium seems also to have an effect on the processing of HEO ceramics since the grain boundary mobility decreases with Li doping due to the segregation, at the grain boundaries, of defects induced by doping.

5.2.2 Temperature dependence. The variation of the real part (ε') of the dielectric permittivity as a function of temperature at various frequencies (20 to 3×10^6 Hz) of $HEOLi_x$ with $0.00 \leq x \leq 0.075$ samples is carefully examined and shown in figure below. It is observed that ε' is frequency and temperature independent at low temperature. Then, it increases gradually with increasing temperature to its maximum value (ε'_{max}) around 423K for $x =$ 0.00, 0.05 and 0.075, respectively, which corresponds to the transition from a ferroelectric to a paraelectric phase. The study of the dielectric constant indicates that for $x =$ 0.00 (Fig 5.4a), the transition temperature value has no variation as a function of frequency, which confirms that these compositions are of classical ferroelectric type.

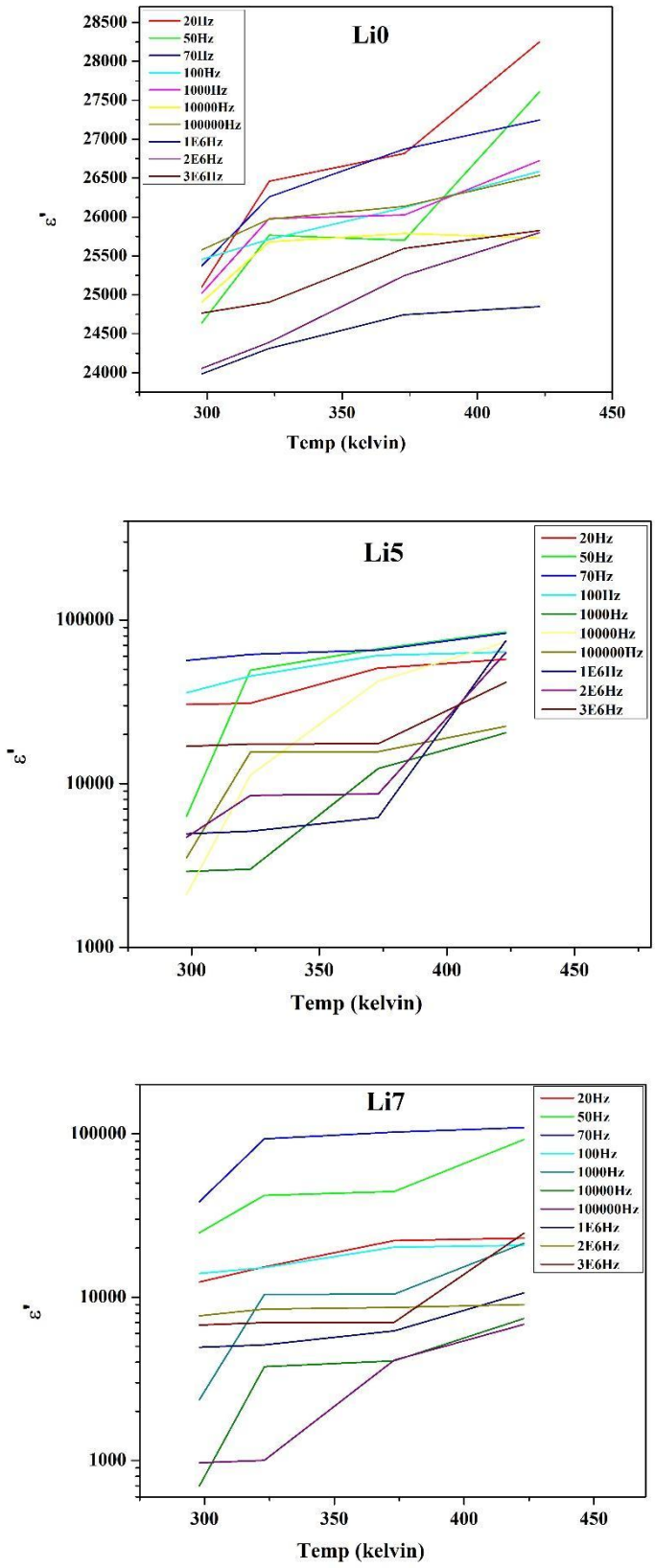

Fig. 5.4 - Temperature dependence of Real Permittivity of Li0, Li5 and Li7

Fig. 5.5 shows the dielectric loss (tan δ) as a function of temperature at various frequencies. The variation of tan δ with frequency shows a similar nature as the variation of ε' with frequency. It is seen from the figure that the dielectric loss initially decreases rapidly with increasing frequency, exhibiting a dispersion at lower frequencies, and then remains fairly constant at higher frequencies. However, with the increase in the frequency of the applied field the mechanisms of polarization such as space charge, orientation, and ions start lagging

behind the field and, thus, dielectric loss decreases. Meanwhile, the variation of the dielectric loss with temperature exhibits the same nature as that of the variation of dielectric constant with temperature and could be explained in the same way as that used for discussing the dielectric constant. It is found that with the increase in temperature, the dielectric loss increases. The mobility of charge carriers increases with temperature which increases the polarization and leads to high dielectric loss. The observed higher value of dielectric loss at high temperature is due to charge accumulation at grain boundaries.

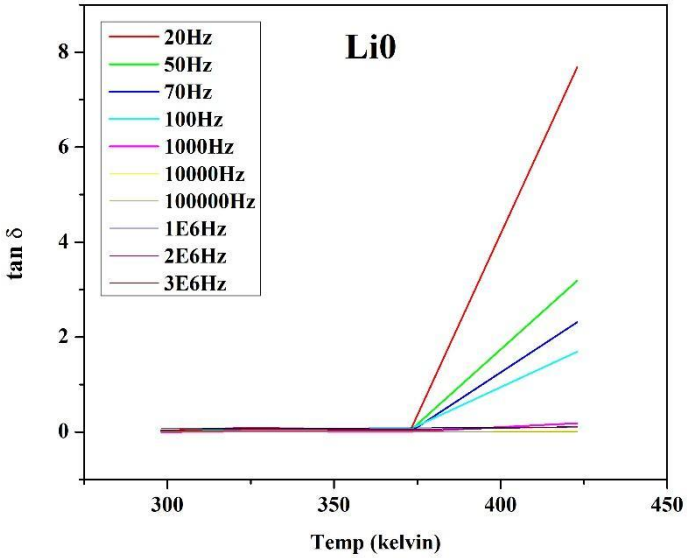

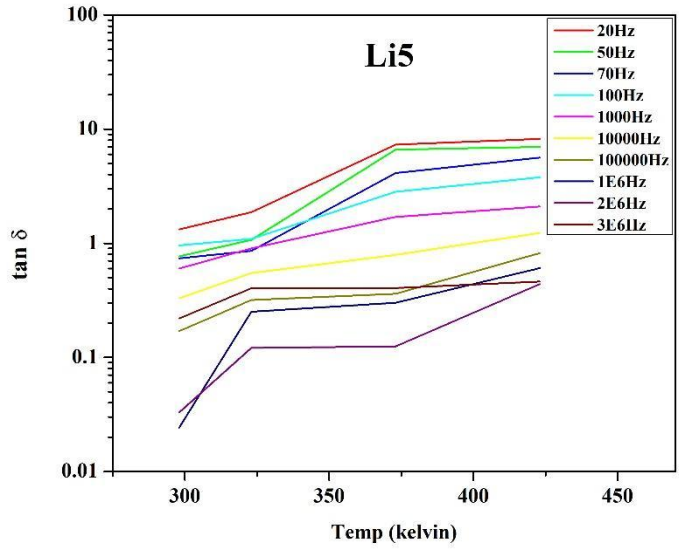

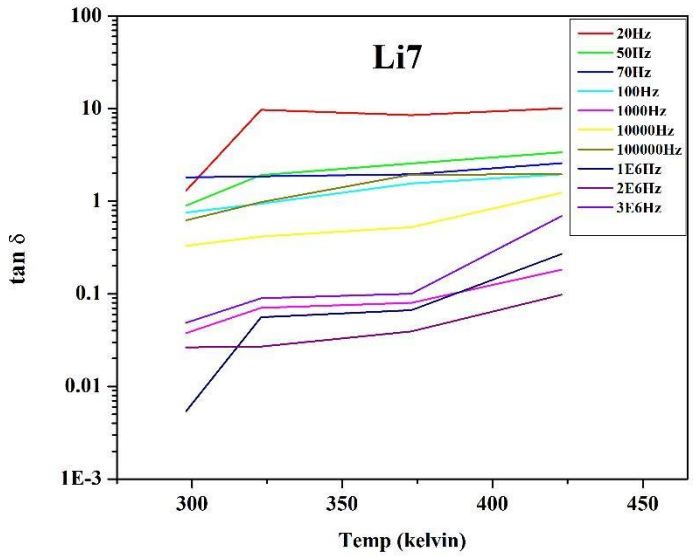

Fig. 5.5 - Temperature dependence of loss factor of Li0, Li5 and Li7

If we summarize as a whole analysis, the direct action of lithium, in this class of materials, can also be seen. Without Li, this parameter remains also equal to unity in a large range of temperatures, whereas it noticeably decreases with the lithium content and becomes sensitive to temperature increase. This is probably related to a larger disorder of the structure, due to the defects that originates from Li substitution(assumption of Schottky defect), leading to a frequency dispersion. We can calculate the "ideal" permittivity. It should be pointed out that the lithium content has again a large impact on the observed values. The less lithium the sample contains, the higher is its intrinsic Impedance and the higher is also its maximum permittivity. Moreover, this maximum is observed at lower temperatures, when the amount of lithium in the material is increasing, which allows, once again, to tailor the dielectric behaviour of these compounds by adapted/controlled lithium doping, opening a wide variety of different uses for example in **energy storage or electronic devices**. The representation of the real part of the" permittivity , as well as the evolution of dielectric loss (tanδ) as function of the frequency, gives some information about the dielectric behaviour of the materials in real/practical conditions. We can observe that the permittivity remains unusually high and stable on a wide range of frequencies (2.3 MHz–1000 Hz), especially for low lithium content samples, and noticeably increases at lower frequencies (<100 Hz) to finally reach large values under DC solicitation. Data for HEOx-Li0, for HEOx-Li5 and for HEOx-Li7 are shown in Fig. 5.1,5.3, 5.4, 5.5 It is noteworthy that & remains larger than ε=500 in the kHz range while keeping a low dielectric loss, of the order of 0.001. We underline that measurements with different blocking electrodes (Cu/sample/Cu) gave similar values of relative permittivity.

REFERENCES

1. Yueqiang Lin, Longhai Zhang, Ya Xiong, Tong Wei, and Zhuangjun Fan : Energy Environ. Mater. 2020, 3, 323–345

   Emad S. Goda , Seungho Lee , Muhammad Sohail , Kuk Ro Yoon : Journal of Energy Chemistry 50 (2020) 206-229
2. Colin D. Wessells, Sandeep V. Peddada, Robert A. Huggins and Yi Cui : Nano Lett. 2011, 11, 5421–5425
3. u W d Q w Ch : ACS App d M t d I t f s 2014 6 6196−6201 5. Atanu Roy, Apurba Ray, Priyabrata Sadhukhan, Samik Saha, Sachindranath Das : Materials Research Bulletin 107 (2018) 379-390
6. Feipeng Zhao, Yeyun Wang, Xiaona Xu, Yiling Liu, Rui Song, Guang Lu, and Yanguang Li : ACS App . M t . I t f s 2014 6 11007−11012
7. Dezhi Yang, Jing Xu, Xiao-Zhen Liao, Yu-Shi He, Haimei Liu and Zi-Feng Ma : Chem. Commun., 2014, 50, 13377
8. Peixun Xiong, Guojin Zeng, Lingxing Zeng and Mingdeng Wei : Dalton Trans., 2015, 44, 16746
9. Dapeng Zhang, Junshu Zhang, Zengxu Yang, Xiaochuan Ren, Hongzhi Mao, Xianfeng Yang, Jian Yang and Yitai Qian : Chem. Commun., 2017, 53, 10556
10. Ping Nie, Jiaren Yuan, Jie Wang,, Zaiyuan Le, Guiyin Xu, Liang Hao, Gang Pang, Yuting Wu, Hui Dou, Xiaohong Yan and Xiaogang Zhang : ACS Appl. Mater. Interfaces 2017, 9, 20306−20312
11. Xiaojuan Zhang , Ping He, Xingquan Zhang , Caixia Li, Huanhuan Liu, Shuai Wang , Faqin Dong : Electrochimica Acta 276 (2018) 92-101
12. Xiaofei Bie , Kei Kubota , Tomooki Hosaka , Kuniko Chihara , Shinichi Komaba : Journal of Power Sources 378 (2018) 322-330
13. Xiao Wang, Baoqi Wang, Yuxin Tang, Ben Bin Xu, Chu Liang, Mi Yana and Yinzhu Jiang : J. Mater. Chem. A, 2020, 8, 3222
14. Anxing Zhou, Liwei Jiang, Jinming Yue, Yuxin Tong, Qiangqiang Zhang, Zejing Lin, Binghang Liu, Chuan Wu, Liumin Suo, Yong-Sheng Hu, Hong Li, and Liquan Chen : ACS App . M t . I t f s 2019 11 41356−41362
15. Samuel Wheeler, Isaac Capone, Sarah Day, Chiu Tang and Mauro Pasta : Chem. Mater. 2019 31 2619−2626
16. Yun Tang , Wei Li , Pingyuan Feng , Min Zhou , Kangli Wang , Kai Jiang : Chemical Engineering Journal 396 (2020) 125-269
17. Yingbo Yuan, Duan Bin, Xiaoli Dong, Yonggang Wang, Congxiao Wang, and Yongyao Xia : ACS Sustainable Chem. Eng. 2020 8 3655−3663

CHAPTER 7 : FUTURE STUDY

In this work four different samples as Li0, Li5, Li7, Li10 were synthesized via reflux method. Some of the characterization procedures such as XRD, FTIR, UV-Vis Spectroscopy (for all samples) and EIS(Dielectric Spectroscopy) (all but Li10 sample) were performed. According to the results obtained from above mentioned procedures were interpreted thoroughly.

Due to inaccessibility of some equipment, few characterization related to my objective was not accomplished. In future, upon accessibility of such instruments I believe the remaining measurements can be acquired with ease.

The remaining measurements of my future studies are as follows :

- Field Emission Scanning Electron Microscopy (FESEM) : To study the morphology and microstructures of Li0, Li5, Li7, Li10 sample.
- High Resolution Transmission Electron Microscopy (HRTEM) : To analyse the crystallographic structure, particle size and defects of synthesized samples.
- Inductively Coupled Plasma Optical Emission Spectrometry (ICP-OES) : To know weight% of the chemical composition present in the synthesized samples to evaluate their chemical formula.
- Thermogravimetric Analysis (TGA) : To study the thermal stability, decomposition kinetics and water content of the synthesized samples.
- X-ray Photoelectron Spectroscopy (XPS) : To study surface chemical properties and bonding natures of the prepared samples.
- Raman Spectroscopy : To study structural analysis of the prepared samples.
- PL (Photoluminescence) Spectroscopy : To investigate optical and electronic properties of prepared samples.
- Electrochemical Analysis : To Study the CV, GCD, EIS properties of as-prepared samples formulating in a coin cell and see the characteristics in case of Supercapacitor and battery separately.
- Liquid Nitrogen : For temperature dependence, negative temperatures below room temperature needs to be done using liquid nitrogen.

CHAPTER 8 : CONCLUSIONS & FUTURE SCOPES

- **Conclusions :**

In the present work, the HEO – (MgNiCuZnCo)O (Li0) and its analogues (Li5,Li7,Li10) materials have been synthesized using co - precipitation procedure. The synthesized samples after being sintered were characterized by X-ray diffraction (XRD), Fourier transform infrared spectroscopy (FTIR), UV-Visible spectroscopy.

The structural study was conducted for XRD in a 2θ mode from 10º to 80º. The XRD pattern for each sample showed corresponding sets of peaks characteristic of Single-phase rocksalt like face centered cubic lattices. The framework crystalline structure constructed with M-O ligands was verified using FTIR analysis. Ultraviolet−visible spectral study was recorded to understand the electronic structure and the optical band gap of the prepared samples.

For the application purpose or being specific dielectric property we choose the dielectric spectroscopy of those prepared samples. The EIS Dielectric Spectroscopy of Li0, Li5, Li7 sample was performed. Li7 delivered the highest dielectric constant of order 1 x 10^5 at 423k around 70Hz. The higher value of lithium doping, higher is the value of dielectric constant. From this, we can conclude that HEOx and its analogues can be an excellent candidate for future energy storage devices for its excellent storage mechanism

- **Future Scopes :**

HEO & HEOAs have proved itself such an excellent material in the field of energy storage device for its different novel properties. Some of the newest approaches in this topic can be done in future are as follows :

a. By varying synthesis condition of (MgNiCuZnCo)O and its lithium analogues, we can perform Rietveld refinement of the prepared samples to obtain its structural information and to study their electrochemical properties in non-aqueous electrolyte.
b. By incorporating conducting polymer (PANI, polypyrrole) material with (MgNiCuZnCo)O and its lithium analogues, we can design asymmetric supercapacitor to investigate improvements on its electrochemical performance.
c. After dielectric measurement there are more aspects to be judged before we certify as a perfect solid electrolyte. Such as electrolyte conductance and dissociation, Ion Solvation, Salt effect, thermal stability,etc.